UiT The Arctic University of Norway

Faculty of Science and Technology
Department of Physics and Technology

Rossby Wave Changes During the Recent Decades in Mid-Latitude Continents in the Northern Hemisphere

Ieva Juskenaite

EOM-3901 Master's thesis in Energy, Climate and Environment
June 2022

This thesis document was typeset using the *UiT Thesis LaTeX Template*.

Abstract

Increasing frequency and severity of extreme weather events throughout the recent years is a highly concerning topic. Extreme and unusual weather conditions, such as heat waves, floods and cold spells are causing a major concern for humanity. Agricultural changes, damages in infrastructure and the loss of human lives are some of the extreme weather event consequences, with the most drastic consequences experienced by the poor and least adaptable groups of society. Recent studies indicate that the increase of extreme weather events can be linked to the effects of global warming, and projections indicate that the frequency and severity of these events is expected to continue increasing in the nearest future. Extreme weather events in mid-latitude continents in the Northern Hemisphere are considered to be linked to atmospheric circulation changes, that are induced by the decreasing meridional temperature gradient due to the effects of Arctic amplification. Atmospheric Rossby waves, in addition to baroclinic cyclones, are considered to be the main factors driving the atmospheric mid-latitude circulation, and recent studies suggest that changes in phase velocity and amplitude of Rossby waves is a indirect consequence of climate change. Here, an attempt to analyse the changes in atmospheric wave amplitudes throughout the recent decades is presented, concentrating on the amplitude tendencies regarding the most extreme amplitude anomalies. This is accomplished by applying Fourier decomposition on a geopotential height field, splitting it into planetary- and synoptic-scaled waves, and further analysing the amplitude changes and tendencies regarding the planetary-scaled Rossby waves. Throughout this studies, no certain amplitude tendencies could be confirmed when regarding all of the planetary waves together, however potential linearly increasing amplitude tendencies could be noted when performing individual Rossby wave analysis.

Acknowledgements

First and foremost I would like to thank Professor Rune Grand Graversen for the endless guidance and support throughout this thesis. Even through hard times, that unfortunately became a large part of this experience, your door was always open and I could always count on your help. Without you, the delivery of this thesis would have been impossible.

I would also like to thank my closest friends and family for all your support throughout this studies, and especially the endless support during the last year. You stood by my side through both good and bad times, and I will forever remain grateful for that.

Finally, I would like to thank my fellow students. This has been an unforgettable experience, thank you all for the great memories.

Contents

List of Figures

List of Tables

1

Introduction

1.1 Background and motivation

Climate change is a highly discussed and researched topic, and the observed and indicated climate change consequences are worrying, especially considering the increased strength and frequency of extreme weather events in the recent years (15). An extreme event is known as a severe and unusual occurrence in weather and climate conditions, that can lead to largely negative impacts on society, agriculture and infrastructure. Even though indications regarding the increasing severity and frequency of extreme weather events have been discussed for a long time, no highly noticeable observations were made until the recent years. In the last years, reports of new extreme weather events are increasing worldwide, and the large media coverage has contributed to increasing interest in the society. News of unexpected heat waves, droughts, floods and cold spells are becoming more frequent, and the consequences caused by these events are devastating (3; 9; 2; 5).

An interesting hypothesis, that we from now on will refer to as extreme event hypothesis, suggests that the indirect effects of global warming are one of the main contributing factors responsible for the increased frequency and severity of extreme weather events in the mid-latitude continents in the Northern Hemisphere (12; 16). The extreme event hypothesis suggests that the rapid warming of the Arctic regions compared to a slower warming of the mid-latitude regions, known as Arctic amplification, is contributing to a decreased meridional temperature gradient and affecting the mid-latitude atmospheric circulation.

Planetary Rossby waves and cyclones are some of the main factors driving the mid-latitude climate, and research shows that changes in the meridional temperature gradient are resulting in Rossby wave meandering and cyclone development changes (13).

As noted above, planetary Rossby waves play an essential role on mid-latitude climate, transporting cold polar air towards the equator and warm tropical air towards the poles, as well as carrying both high and low pressure weather systems throughout mid-latitudes. Changes in Rossby wave properties, such as the wave amplitude and propagation velocity, are contributing to different mid-latitude climate phenomenons, including the development of extreme weather events. Since Rossby waves transport cold and warm air throughout mid-latitudes, Rossby wave phase velocity relates to the time cold or warm air hovers over a certain mid-latitude region. Weaker meridional temperate gradient indicates a decrease in the phase velocity of atmospheric Rossby waves, leading to certain weather conditions stalling over a region for a longer period of time, lasting over several days or even several weeks (16). Prolonged weather conditions over the same region can lead to development of extreme weather events: warm tropical air stalling over a region can develop droughts and heat waves, while cold polar air stalling over a region can develop into cold spells.

In addition to the slower Rossby wave phase speed, extreme event hypothesis indicate that decreasing meridional temperature gradient is also resulting in larger Rossby wave amplitudes (12). Based on this hypothesis, the motivation of this thesis is to analyse Rossby wave changes over the recent decades, mostly regarding changes in the wave amplitude, and examine if any clear amplitude tendencies can be noticed during the past decades. Since our project paper analysis concentrated on the cold spells in Europe during the winter of 2021/2022, see section 1.2, we will analyse amplitude tendencies occurring specifically throughout the winter months only, such that further work connecting the potential amplitude tendencies to potential cold spells could easily be achieved.

1.2 Summary of project paper

In the project paper "Cold Spells over Mid-Latitude Continents During Northern Hemisphere Winter of 2020-2021", which acted as the introduction to this thesis, we analysed a specific cold spell event that took place in Acropolis, Greece, and Houston, Texas, USA during February 2021, where both Acropolis and Houston simultaneously experienced unusually low temperatures and large amounts of snow (4; 6). The goal of the project exercise was to investigate if surface air temperatures were indeed unusually low during the February 2021 cold spell event compared to the climatology of the area, and if the 500 hPa geopotential height field indicated cold polar air supply towards Acropolis and Texas during the cold spell event. We here take a quick review of results.

By using SAT data from ERA5 provided by ECMWF database, we calculated temperature anomalies of February 2021 relative to the February climatology calculated based on the 1979-2020 February SAT data, for both Acropolis, see fig. 1.3a, and Houston, see fig. 1.3b. From the temperature anomalies we could confirm that both Acropolis and Houston experienced unusually low temperatures in approximately same time period, and we used the result to estimate that the cold spell took place between 13th-17th of February 2021.

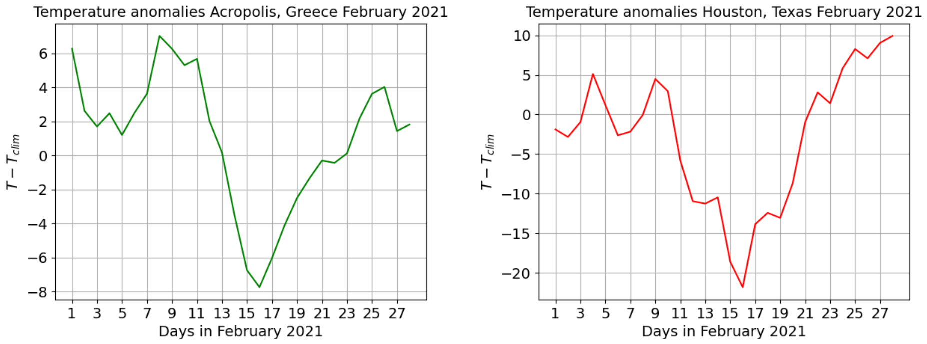

(a) **(b)**

Figure 1.1: Temperature anomalies in C°representing daily February 2021 temperatures relative to 1979-2020 February climatology. (a) Temperature anomalies for Acropolis, and (b) temperature anomalies for Houston.

Once a common time period for cold spells in Acropolis and Houston was confirmed, 13th-17th of February, we proceeded to calculate global temperature anomalies between temperatures at the time of cold spell event relative to the 1979-2020 February climatology, see fig. 1.2. Results indicate that both Northern America, Eastern Europe and Northern Russia were experiencing unusually low temperatures relative to their climatology, that could also be confirmed when comparing temperatures to standard deviation, most likely indicating possible cold spell events in these areas.

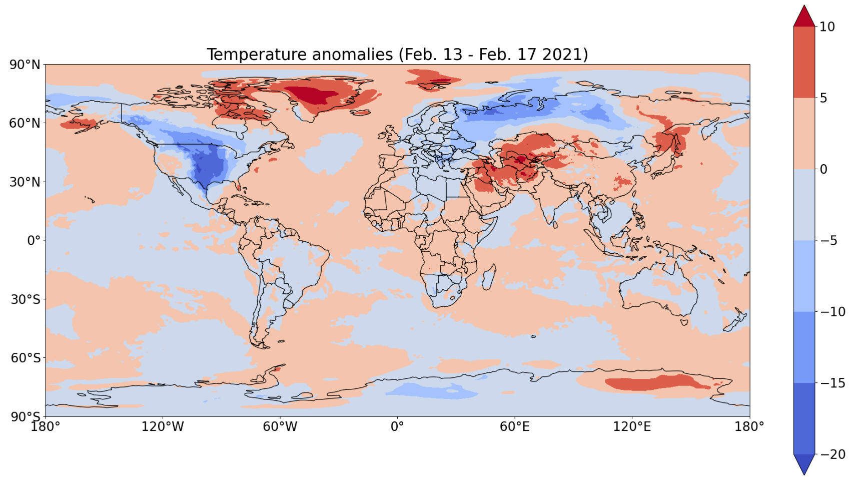

Figure 1.2: Global surface air temperature anomalies in C°, indicated by different color shades, representing temperatures at the time frame of cold spell event relative to 1979-2020 February climatology. Red shading indicates temperature anomalies above 0, while blue shading indicates temperature anomalies below 0.

Since large negative temperature anomalies were confirmed in our regions of interest, Northern America and Europe, we plotted the corresponding 500 hPa geopotential height field over the same areas to investigate atmospheric circulation patterns, see fig. 1.3.

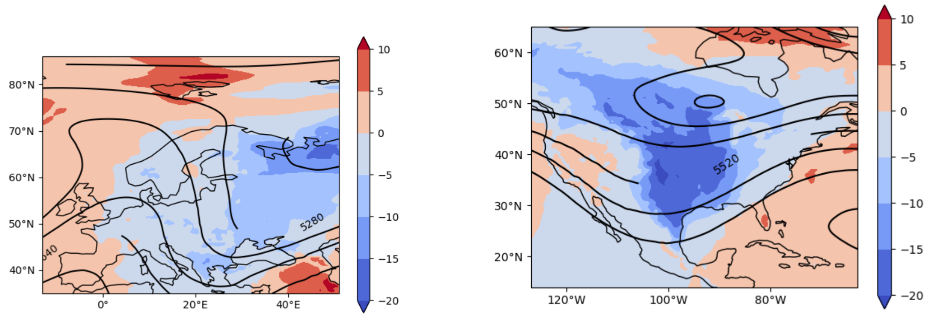

(a) **(b)**

Figure 1.3: Temperature anomalies in C°representing cold spell event temperatures relative to 1979-2020 February climatology. Black lines indicates corresponding lines of the 500 hPa geopotential height field, where contour interval is set to 120m. Temperature anomalies and corresponding geopotential field lines are plotted for both (a) Europe, and (b) Northern America.

Contours of 500 hPa geopotential height field lines, provided in the figure above, indicate a large-scale atmospheric circulation where cold polar air reaches all the way down to the latitudes of Acropolis and Houston, explaining the extremely low temperatures experienced by these regions. Upcoming calculations and discussions in this theses are based on the results from the project exercise.

2

Background Theory

2.1 Basic fluid dynamics equations

To be able to explain and study different phenomenons in the atmosphere, we have to introduce some of the main fluid equations, as these basic equations describe how different forces and temperatures can affect a fluid's flow.

From the classical (solid) mechanics we are familiar with conservation of mass, and that mass can neither be created or destroyed. However, when we are work with classical mechanics, we most of the time use Lagrangian point of view, also referred to as material point of view, meaning that we follow e.g. a parcel through time and space. In situations like these we are considering motion of a parcel that has a constant mass, and it therefore is unnecessary with mass conservation equations. When we work with fluid dynamics, it is much more common to use a Eulerian point of view (even though Lagrangian view can be applied, and it is important in developing the equations), also referred to as field point of view, where we choose a fixed area in space and check how e.g. velocities and densities change inside that fixed area with time. Since a fluid is flowing through the area, both density and velocity might change, meaning that we need an equation that can express mass conservation, which leads to the following mass continuity equation:

$$\frac{D\rho}{Dt} + \rho \nabla \cdot \boldsymbol{v} = 0 \tag{2.1}$$

where D/Dt is the material derivative, ρ is density and $\boldsymbol{v} = \boldsymbol{v}(u, v, w)$ is the flow velocity.

Another important aspect when working with fluid dynamics is describing fluid motion when it is affected by different forces. Forces such as pressure and gravity can affect both the velocity and the momentum of a fluid, and the following momentum equation describes how different forces and fluid motion is connected together in a rotating fluid:

$$\frac{D\boldsymbol{v}}{Dt} = -\frac{1}{\rho}\nabla P - f\hat{k} \times \boldsymbol{v} - g\hat{k} + F \tag{2.2}$$

where P is the pressure force, $f = 2\Omega\sin\phi$ is the Coriolis parameter, g is gravity acceleration constant and F are other forces, e.g. friction and dissipation. It is common to both look at the momentum equation as a one combined equation, such as in equation 2.2, or to split it up into horizontal and vertical momentum equations respectively as following:

$$\frac{D\boldsymbol{u}}{Dt} = -\frac{1}{\rho}\nabla_z P - f\hat{k} \times \boldsymbol{u} \tag{2.3}$$

$$\frac{D\boldsymbol{w}}{Dt} = -\frac{1}{\rho}\frac{\partial P}{\partial z} - g \tag{2.4}$$

where $\boldsymbol{u} = \boldsymbol{u}(u, v, 0)$ is the horizontal flow velocity and $\boldsymbol{w} = \boldsymbol{w}(0, 0, w)$ is the vertical flow velocity.

2.2 Hydrostatic balance

Hydrostatic balance is a type of vertical fluid approximation, that is commonly used when working with both ocean and atmosphere. Equation for hydrostatic balance can be derived by using two different methods, either by scaling the vertical momentum equation or by assuming that fluid is static in the vertical direction. When using the scaling method, we scale all of the therms in the vertical momentum equation by using typical values from "real-life" scenarios, and neglecting the terms that have smaller magnitude than the rest of the terms in the equation; or in other words, neglecting terms that are of a smaller importance. Instead of using the scaling method, it is also possible to assume that the fluid is static in the vertical direction, implying that the acceleration in the vertical direction is zero, and therefore $\frac{Dw}{Dt} = 0$. Both of these approaches yield that the hydrostatic balance can be expressed as the following equation:

$$\frac{\partial P}{\partial z} = -\rho g \tag{2.5}$$

Due to dynamics of the atmosphere, we know that in large-scale atmospheric flows the vertical acceleration is small compared to pressure and gravity, which leads to hydrostatic balance being an excellent approximation when working with the large-scale atmosphere. Hydrostatic balance might not be such a great approximation regarding small-scale atmospheric flows, e.g. fronts, but here we will mostly be concentrating on the large-scale atmospheric motions.

2.3 Geostrophic balance

Geostrophic balance is an important simplification that tell us how pressure field and velocities relate to each other, in situations where Coriolis force is much larger than inertial forces. To check if geostrophic balance can be applied to our situations of interest, we introduce Rossby number, that identifies significance of fluids' rotation. To find the Rossby number, we scale the horizontal momentum equation (eq. 2.3), and find the ratio between the Coriolis term and the advective term. We define this ratio as the Rossby number, and it can be expressed as:

$$R_0 = \frac{U}{fL} \tag{2.6}$$

where R_0 is the Rossby number, U is the typical horizontal velocity scale (for atm.: $\approx 10ms^{-1}$) and L is the typical horizontal length scale (for atm.: $\approx 10^6$ m). If a fluid is strongly affected by the Coriolis force, the Coriolis parameter is going to be large and the Rossby number is going to be small (for atm.: $R_0 \approx 0.1$). This tells us that the advective term is smaller than the Coriolis term, and can therefore be neglected. If we then in addition apply advective time scaling, we achieve geostrophic balance. In practise, it implies that the pressure term is the only term of relevance when balancing out the Coriolis term, and the geostrophic balance can therefore be expressed as

$$\boldsymbol{f u} \approx -\frac{1}{\rho}\nabla_z P \tag{2.7}$$

which can also be split into components as

$$fu \approx -\frac{1}{\rho}\frac{\partial P}{\partial y}, \qquad fv \approx \frac{1}{\rho}\frac{\partial P}{\partial x} \tag{2.8}$$

2.4 Thermal Wind Balance

Thermal wind, as opposed to what the name would suggest, is not actually a wind but rather a difference between winds at two different heights along constant pressure levels. Let us look at what happens at a polar front, where cold, Arctic air meets warm, subtropical air. Since warm air is less dense than cold air, it takes up more space compared to cold air. This means that a pressure level of e.g. 500 hPa is going to be higher above the surface at the warm side of the polar front compared to the cold side of the polar front. For this to hold true, the pressure has to change rapidly over the polar front, creating large pressure gradient force that point towards the north in the Northern Hemisphere (and towards the south in the Southern Hemisphere). It is this pressure gradient force that set the wind in motion, and due to Earth's rotation and Coriolis force, these winds get deflected towards the east. In other words, thermal wind explains how change of temperature in the meridional direction will change winds' magnitude and direction.

In a more mathematical way, thermal wind can be expressed as the vertical derivative of geostrophic wind, and the thermal wind balance arises by combining the hydrostatic and geostrophic approximations (18, p. 91). Thermal wind balance is commonly expressed by either using the Boussinesq or anelastic approximations, where the mean density is either assumed to be constant (as in the Boussinesq approximation) or varying with height (as in anelastic approximation), in addition to small perturbations in all directions. The Boussinesq approximation simplifies that density and pressure, that are assumed to be in hydrostatic balance, can be expressed as

$$\rho = \rho_0 + \delta\rho \qquad\qquad P = P_0(z) + \delta P \tag{2.9}$$

where ρ_0 is mean density, $\delta\rho = \delta\rho(x, y, z, t)$ is a small density perturbation, $P_0(z)$ is the pressure following from hydrostatic balance and $\delta P = \delta P(x, y, z, t)$ is a small pressure perturbation. Given the definition of perturbation we assume that $|\rho_0| >> |\delta\rho|$ and $|P_0| >> |\delta P|$. In addition, following the definition of hydrostatic balance (eq. 2.5), density and pressure can be related together as

$$\frac{dP_0}{dz} = -g\rho_0. \tag{2.10}$$

In a similar manner, the anelastic approximation simplifies that the density and pressure can be expressed:

$$\rho = \tilde{\rho}(z) + \delta\rho \qquad\qquad P = \tilde{P}(z) + \delta P \tag{2.11}$$

where $\tilde{\rho}(z)$ is density as a function of height and $\tilde{P}(z)$ is the pressure following from hydrostatic balance. Here is is also assumed that $|\tilde{\rho}(z)| >> |\delta\rho|$ and $|\tilde{P}(z)| >> |\delta P|$, as well as that pressure and density are in hydrostatic balance, and can therefore be related as

$$\frac{\partial\tilde{P}}{\partial z} = -g\tilde{\rho}(z). \tag{2.12}$$

In real life scenarios, we can apply the Boussinesq and anelastic approximations when working with the ocean and atmosphere. Since Boussinesq approximation assumes a mean density, and density variations in the ocean due to changes in salinity and thermal expansion are minimal, the Boussinesq approximation can with quite high accuracy be applied to oceans. However, density throughout the atmosphere can not be considered constant, specially in the vertical direction, as affects of gravity and molecular structure leads to large variations in density. Therefore, the Boussinesq approximation is not valid for the atmosphere, and the anelastic approximation is a much better fit, where density is expressed as a function of height.

Since we are mostly interested in how thermal wind balance applies in the atmosphere, we use the anelastic approximation on both the hydrostatic and geostrophic balance, and can therefore express the hydrostatic balance as eq. 2.12 and the geostrophic balance as

$$fu = -\frac{1}{\tilde{\rho}(z)}\frac{\partial \tilde{P}}{\partial y} = -\frac{\partial \phi}{\partial y}, \qquad fv = \frac{1}{\tilde{\rho}(z)}\frac{\partial \tilde{P}}{\partial x} = \frac{\partial \phi}{\partial x} \tag{2.13}$$

where $\phi = \partial\tilde{P}/\tilde{\rho}(z)$. By defining buoyancy, b, as $b \equiv -g\,\partial\theta/\theta_0$, where θ is the potential temperature, we can also rewrite eq. 2.12 as

$$\frac{\partial \phi}{\partial z} = b. \tag{2.14}$$

By combining the anelastic approximation, hydrostatic balance and geostrophic balance provided by eqs. 2.13 and 2.14, we get that thermal wind balance can be expressed as

$$\frac{\partial u}{\partial z} = -\frac{1}{f}\frac{\partial b}{\partial y} = \frac{g}{f\theta_0}\frac{\partial(\partial\theta)}{\partial y}, \qquad \frac{\partial v}{\partial z} = \frac{1}{f}\frac{\partial b}{\partial x} = -\frac{g}{f\theta_0}\frac{\partial(\partial\theta)}{\partial x}. \tag{2.15}$$

From equations above we see that given no change in temperature, the temperature gradient would become 0, yielding that there would be no wind shear (winds would not change with height). However, if the temperature gradient is different from 0, it indicates that we have a wind shear, meaning that zonal wind speeds would either increase or decrease with height, depending on the sign of temperature gradient.

2.5 Baroclinic and barotropic fluids

Fluids can be split into two different categories, baroclinic or barotropic fluids, depending on how isobars (lines of constant pressure) and isopycnals (lines of constant density) interact with each other. Assume that we have a barotropic fluid, where isobars and isopycnals are oriented such that they are parallel to each other. This implies that along constant pressure lines, the density remains constant. We then define the ideal gas law as

$$P = \rho RT \tag{2.16}$$

where R is the ideal gas constant and T is the temperature. Since both density and pressure in a barotropic fluid are constant, it implies that temperature has to be constant as well and that pressure in a barotropic fluid is a function of density alone, $P = P(\rho)$. By applying this to the thermal wind balance equation, eq. 2.15, we notice that given a barotropic atmosphere the temperature gradient is going to be zero, and there will be no vertical wind shear.

We now assume that we have a baroclinic fluid, where isobars and isopycnals intersect with each other, meaning that density is changing along a constant pressure line. Ideal gas law implies that in a baroclinic fluid pressure is a function of both density and temperature, $P = P(\rho, T)$ and implies that in a baroclinic atmosphere winds are changing as a function of heights, since the temperature gradient is different from zero.

To implement this to the Earths' atmosphere, we have to think about the magnitude of the temperature gradient at different latitudes. Since the temperature gradient is smallest close to the equator, and is increasing in magnitude towards the poles, it implies that atmosphere in the tropics can be approximated to be a barotropic atmosphere, while atmosphere at the poles mostly represents a baroclinic atmosphere. In mid-latitudes, the situation is more complex, as the atmosphere can be in both baroclinic and barotropic states. However, it is common that baroclinic instabilities occur in the mid-latitude atmosphere creating baroclinic eddies, that together with Rossby waves are an essential part of mid-latitude circulation.

2.6 One-layer shallow water system

Working with the dynamics of a fluid, in our case atmosphere, can be complicated as different processes in the atmosphere can be complex and be highly dependent on each other. Since the processes in the atmosphere interact with many different variables, there are multiple equations that are needed to provide enough information and to solve a problem; E.g. it is quite common to use both thermodynamical equation and the equation of state, in addition to momentum and continuity equations, to derive a solution for an atmospheric system. However, we are interested in making our derivations as simple as possible that still can be approximated to real-life scenarios, therefore using shallow water approximation is optimal when working with different waves in the atmosphere.

Shallow water system is a highly simplified system that allows us to derive e.g. dispersion relations and phase and group velocities of different types of atmospheric waves (e.g. Rossby, gravity and Kelvin waves) using only the momentum and continuity equations, as well as providing results that can be approximated to real-life problems. We consider a situation with a one-layer fluid, illustrated in figure 2.1, where the horizontal length scale, H, is assumed to be much larger than the vertical length scale, L, such that the effects of stratification can be ignored. In other words, we assume that fluid density stays constant with height throughout the fluid layer, $\rho = \rho_0$, and due to the length scale difference and corresponding scaling of the continuity equation, we can assume that the magnitude of horizontal velocities are much higher compared to the magnitude of vertical velocities, implying assumption of hydrostatic balance. In addition, we define that the surface topography is denoted by η_S(x, y, t), bottom topography is denoted by η_B(x, y, t) and the height difference between the surface and bottom topography is denoted by h.

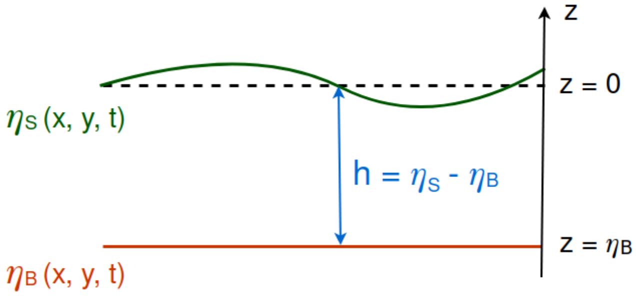

Figure 2.1: Setup of a one-layer shallow water system.

By using assumptions stated above and information given in figure 2.1, we can rewrite the continuity equation, eq. 2.1, into shallow water continuity equation

$$\frac{Dh}{Dt} + h\nabla \cdot \mathbf{u} = 0, \tag{2.17}$$

and rewrite the momentum equation, eq. 2.2, into shallow water momentum equation

$$\frac{D\mathbf{u}}{Dt} + \mathbf{f} \times \mathbf{u} = -g\nabla\eta_S. \tag{2.18}$$

As the goal of this thesis is to investigate mid-latitude circulation trends, which highly depend on propagation of Rossby waves (see ch. 3.1 and 3.2), we use shallow water continuity and momentum equations to investigate Rossby wave propagation. In particular, we are interested in how potential vorticity (PV) can be expressed using the simplifications of a one-layer shallow water system, as background gradient of PV impacts Rossby wave propagation.

To derive the shallow water PV equation, we first apply following vector identity on the shallow water momentum equation

$$(\mathbf{u} \cdot \nabla)\mathbf{u} = \frac{1}{2}\nabla(\mathbf{u} \cdot \mathbf{u}) - \mathbf{u} \times (\nabla \times \mathbf{u}), \tag{2.19}$$

take the curl of the result, and apply following vector identity

$$\nabla \times (\mathbf{A} \times \mathbf{B}) = (\mathbf{B} \cdot \nabla)\mathbf{A} - (\mathbf{A} \cdot \nabla)\mathbf{B} + \mathbf{A}(\nabla \cdot \mathbf{B}) - \mathbf{B}(\nabla \cdot \mathbf{A}). \tag{2.20}$$

Some of the terms automatically is canceled, due to factors such as the vertical component of vorticity being independent of changes in x- and y-direction and that divergence of a curl is equal to 0. Therefore the result, also known as the vorticity equation, can then we expressed as

$$\frac{D\zeta}{Dt} = -\zeta\nabla \cdot \mathbf{u} \tag{2.21}$$

where $\zeta = \partial_x v - \partial_y u$ is the relative vorticity. Since vorticity is not a conserved unit, even in a shallow water model, we want to combine the result together with the shallow water continuity equation. By manipulating the continuity equation, and combining it together with eq. 2.21, the shallow water PV equation can be expressed as

$$\frac{DQ}{Dt} = 0 \tag{2.22}$$

where $Q = (\zeta + f)/h$ is the potential vorticity. From expression above we notice that PV is a conserved unit, that depends on both the relative vorticity and fluid layers height. In chapter 3.2.1 we will be using the shallow water PV equation to derive dispersion relation, as well as phase and group velocity of Rossby waves.

It is worth mentioning that the shallow water model is a better approximation when working with waves in the ocean compared to waves in the atmosphere, as the basis of shallow water approximation is to assume a homogeneous layer, where density stays constant throughout the height of the layer. Since water is nearly incompressible, the pressure force does not have a large effect on the density properties of water, so that the density throughout the ocean can be approximated to be constant. On the other hand, due to the properties of a gas, air is considered to be compressible, with highest air density at low altitudes and lowest air density at high altitudes. Due to compressibility properties of water and gas, the shallow water model is a accurate representation for the ocean, while it deviates from reality for the atmosphere. A solution to applying shallow water model for atmospheric Rossby waves would be to introduce anelastic conditions, see ch. 2.4, where mean density can be expressed as a function of height, together with small perturbations, and to apply a reduced gravity model, where we consider multiple fluid layers of different density stacked on top of each other. However, to keep derivations as simple and tidy as possible, we will use one-layer shallow water model when examining the structure and propagation of atmospheric Rossby waves.

3

Global atmospheric circulation

At any time of the day, there are multiple different weather systems that can be found throughout the Earth, and at first glance it might seem like these weather systems are randomly generated and distributed throughout the globe. However, if weather systems had no specific distribution pattern, it would be highly improbable that most of Earths' biomes could be found at specific ranges of latitudes; for instance that most of Earths' warm deserts and rain forests are located at low latitudes, while most of the tundras and taigas can be found at high latitudes (8). If we average the weather systems throughout the Earth over time, say several years, a global atmospheric circulation pattern emerges.

Solar radiance is the Earths' main source of heat, however due to factors as the tilt and the shape of the Earth, the solar radiance is not distributed evenly throughout the globe. Equatorial regions receive most of the heat, and therefore have the highest temperatures throughout the Earth, while the polar regions receive the least amount of heat, and as a result have low temperatures and are covered in snow and ice. If we look at the Earth as a whole, we notice that Earths' temperature varies highly with latitude, as warmest temperatures are located at the equator and lowest temperatures are located at the poles. Due to the large difference in temperatures at low and high latitudes, we have a large meridional (poleward) temperature gradient. The magnitude of the meridional temperature gradient changes greatly depending on the season; in the winter months, the meridional temperature gradient is larger compared to the meridional temperature gradient during the summer months, as the Northern Pole experiences polar nights and receives approximately no direct solar radiation (18, p. 514). The existence of meridional temperature gradient induces a meridional energy transport, can also be referred to as the global atmospheric circulation, that transports warm tropical air from the equator towards the poles, in attempt to even out the temperatures throughout the globe.

The global atmospheric circulation can be explained by a combination of three circulation cells, known as Hadley, Ferell and Polar cells, that can be found both in the Northern and in the Southern Hemisphere, as illustrated by the figure 3.1:

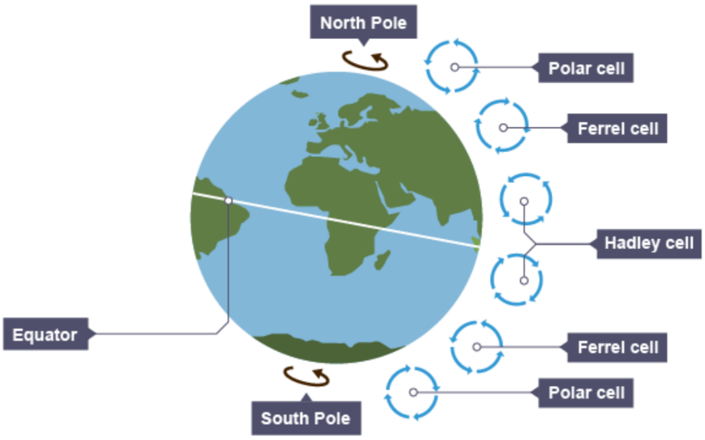

Figure 3.1: Illustration of the global atmospheric circulation (1).

From the figure above we notice that the circulation cells are distributed in the same order both in the Northern and the Southern Hemisphere, with Hadley circulation cell transporting the air closest to the equator and Polar circulation cell transporting the air closest to the poles, however the cell air circulation direction differs in the Northern and the Southern Hemisphere. For the purpose of this exercise, we from now on concentrate on the Northern Hemisphere and take a quick look at the mechanics of the different circulation cells, before we concentrate on the main factors regarding mid-latitude atmospheric circulation.

3.1 Atmospheric circulation cells

Referring back to figure 3.1, we remember that the global atmospheric circulation in the Northern Hemisphere can be split up into three different cells: Hadley, Ferrel and Polar cells. The air circulation in these cells takes place throughout the troposphere, which is an atmospheric layer that extends all the way from the surface and up to 6-20 km in height, where the troposphere is at its highest ($\approx$ 20 km) at the equator, and its lowest ($\approx$ 6 km) at the poles (7). We also notice that the atmospheric circulation cells do not have the same circulation direction when compared to each other, as the ascending (warm) air in Hadley and Polar cells is transported towards the north, while the ascending (cold) air in the Ferrel cell is transported towards the south. Since it is the warm air that is ascending and cold air that is descending in Hadley and Polar circulation cells, they are known as thermally direct cells. The Ferell circulation cell on the other hand is known as thermally indirect cell, where cold air is ascending, while the warm air descends. We take a quick look at each of the atmospheric circulation cells separately.

The Hadley circulation cell is the largest of the atmospheric circulation cells and is the dominating factor of the meridional energy transport in the tropics, where it extends all the way from the equator (0° latitude) and up to approximately 30° latitude. Due to the poleward temperature gradient and the heating of the surface, the air at the equator rises up through the troposphere and is transported towards the north. The farther from the equator the air is transported, the lower are the surrounding temperatures, and at around 30° latitude the air to descends towards the surface and in the end propagates towards the equator, completing the cycle. In addition, due to the rotation of the Earth and the effect of the Coriolis force, the propagating air gets deflected towards the right in the Northern Hemisphere (or towards the left in the Southern Hemisphere), creating different wind systems such as trade winds that occur at low altitudes, and subtropical jet streams that occur at high altitudes (18, p. 537).

In contrast, the Polar circulation cell is the smallest and weakest out of all atmospheric circulation cells, and is ranging from approximately 60° latitude and all the way to the Northern Pole (90° latitude). The general mechanics of the Polar circulation cell are very similar to the Hadley circulation cell; the air propagating towards the Northern Pole at high altitudes is cooled down due to decreasing temperatures, leading the air to descend towards the surface and propagate back towards the equator. At approximately 60° latitude, the cold, polar air mixes together with the incoming warmer air, that is transported from the tropical regions, and rises through the troposphere, where in the end it propagates towards the Northern Pole and completes the cell circulation.

In addition to Hadley and Polar cells, we also have the Ferell cell, that extends from approximately 30° latitude to approximately 60°latitude. In the Ferell cell, it is the cold polar air that rises to higher altitudes and propagates towards the equator while the warmer air descends and propagates towards the Northern Pole. However, the illustration of the Ferell cell gives a misleading understanding of the circulation pattern in the mid-latitude regions, as the Ferell cell circulation is an average of all circulation in the mid-latitude atmosphere, where the circulation is dominated by eddies. In some situations, for instance when studying atmospheric circulation patterns in low latitude regions, we can assume a steady large-scale atmospheric circulation, where eddies are almost negligible. However, the atmospheric circulation in mid-latitudes is almost entirely dominated by baroclinic eddies and large-scale atmospheric planetary waves, and since eddies are chaotic and random, the mid-latitude atmospheric circulation can not be assumed to be steady, but rather turbulent in nature (18, p. 539).

For the purpose of this exercise we are mainly interested in mid-latitude atmospheric circulation, and will therefore take a further look into how baroclinic eddies, mainly cyclones, and large-scale atmospheric Rossby waves, also known as planetary waves, are dominating the mid-latitude circulation.

3.2 Mid-latitude atmospheric circulation

As previously discussed, global atmospheric circulation and meridional energy transport are responses to large differences in temperatures between the equator and the poles. If we were to image a situation, where the Earth did not rotate, a simple solution to reducing the large temperature gradient in the Northern Hemisphere would be a one large atmospheric circulation cell, going all the way from the equator and to the North Pole. In this cell, the cold and Polar winds would be transported to the equator in a form of surface winds, and the heated up air would rise and propagate back to the North Pole. However, we know that Earth does indeed rotate, and the rotation induced Coriolis force has a large effect on the atmospheric circulation, where as a response to the Coriolis force winds in the Northern Hemisphere get deflected towards the right (towards the left in the Southern Hemisphere). As a matter of fact, due to the shape of the Earth, the Earths rotational speed is at its highest at the equator and at its lowest at the Poles, leading to the effects of the Coriolis force being at its lowest at the equator (usually approximated to be non-existent) and increasing in magnitude towards the poles. In other words, as Coriolis force is approximately 0 at the equator, winds are not deflected towards the right in the Northern Hemisphere; however, the higher increase in latitude, the larger Coriolis force the winds are experiencing, meaning that the magnitude of wind deflection is increasing together with increase of latitude.

The effect of Coriolis force is one of the main reasons to creation of Rossby waves and eddies, that are dominating the mid-latitude atmospheric circulation. During this thesis, we will be studying the behaviour of Rossby waves in the mid-latitude atmosphere, therefore we will now take a more detailed look at the development and propagation of Rossby waves, and its affect on the mid-latitude climate. We will in addition take a quick look at the development of mid-latitude cyclones, as they play an important role to weather changes in mid-latitude continents.

3.2.1 Atmospheric Rossby waves

In the mid-latitudes, Rossby waves are one of the most dominant circulation pattern present in the general atmospheric circulation. Rossby waves form due to the Earth rotation, and may be developed by orographic effect or land-ocean heating contrasts. Both of these effects results in a meandering of the east-west flow.

Since the motion of the Rossby waves are closely linked to climate and mid-latitude patterns it is of high importance to understand its motion and meandering. The motion of Rossby waves can be clearer understood by analysing the development of Rossby waves. This Rossby wave motion can be described by the derivation of the dispersion relation, in a simplified and idealised atmospheric state.Consider a single layer system in a shallow water model, the quasi-geostrophic PV equation, provided by equation 2.22, can be expressed as

$$\frac{D}{Dt}\left[\zeta + f - k_d^2\psi\right] = 0 \tag{3.1}$$

where ζ is the relative vorticity, f is the Coriolis parameter and $k_d = 1/L_d$ is the inverse radius of deformation (Rossby radius) for a shallow water system. Considering the deformation radius , we assume an infinite deformation radius, meaning that the length scale of the perturbations/disturbances we are considering are much smaller than the scale of the deformation radius, L_d. In such cases we can as a good approximation neglect the term $k_d^2\,\psi$ in equation 3.1 as the inverse radius of deformation $k_d \approx 0$.

To describe mid-latitude wave motions where we consider effects of Earths geometry, we introduce the beta approximation, that let us vary the Coriolis parameter with latitude. The planetary vorticity can then be expressed as $f = f_0 + \beta y$, where f_0 is constant and dependent on the initial latitude. Inserting this into equation above, we can rewrite eq. 3.1 as

$$\frac{D}{Dt}[\zeta + \beta y] = 0 \tag{3.2}$$

The instability for perturbations ψ can be deduced by linearizing about a constant zonal flow A, and can be expressed as

$$u = A(x) + u'(x, y, t), \quad v = v'(x, y, t), \quad \psi = \Psi(y) + \psi'(x, y, t), \tag{3.3}$$

where the zonal flow A can be represented by a streamfunction $\Psi = -Ay$. In addition, the streamfunction and vorticity is related together as

$$\left.\begin{aligned} u' &= -\tfrac{\partial}{\partial y}\psi' \\ v' &= \tfrac{\partial}{\partial x}\psi' \end{aligned}\right\} \implies \qquad \zeta = \nabla^2\psi'$$

From this, the linear equation in perturbation streamfunction ψ is given by

$$\left(\frac{\partial}{\partial t} + A\frac{\partial}{\partial x}\right)\nabla^2\psi' + \beta\frac{\partial}{\partial x}\psi' = 0 \tag{3.4}$$

where the terms containing products of perturbations were neglected. The resulting equation is a differential equation, and a solution is sought after in the form of a plane wave on the form of

$$\psi' = Re\left[\tilde{\psi}e^{i(kx+ly-\omega t)}\right] \tag{3.5}$$

where $\tilde{\psi}$ is a complex constant which is not dependent on time or space. k and l are wave numbers for x- and y-direction respectively, while the oscillation frequency is defined as ω. Inserting the plane solution into the differential equation, eq. 3.4, we find that the dispersion relation can be exressed as

$$\omega = k\left(A - \frac{\beta}{(k^2 + l^2)}\right) \tag{3.6}$$

Equation above is the dispersion relation for barotropic Rossby waves. The dispersion relation can be used to express the phase speed for x- and y-direction by dividing it for the corresponding wave number in the given direction. For our case we are interested in the zonal wave speed direction , consequentially expressing our phase speed as

$$c_x = \frac{\omega}{k} = A - \frac{\beta}{(k^2 + l^2)} \tag{3.7}$$

where c_x is the zonal phase speed. It can be noticed that the parameter is dependent on the wave number which leads to the understanding that the Rossby waves are dispersive. With no mean background flow, A = 0, Rossby waves is expected to have a westward propagation. If the background flow is A = $\beta/(k^2+l^2)$ the waves would be stationary. For an even better understanding of the waves and its movements, the group velocities in the zonal direction should be considered, and can be expressed as

$$c_g = \frac{\partial\omega}{\partial k} = A + \frac{\beta(k^2 - l^2)}{(k^2 + l^2)^2} = c_x + \frac{2\beta k l}{(k^2 + l^2)^2} \tag{3.8}$$

Observing the Rossby wave group velocity in the zonal direction, we notice indications of faster eastward propagation relative to the corresponding phase speed. In addition, we notice that stationary waves can only propagate eastward, also affecting downstream development of Rossby wave packets.

If we instead consider a situation with a finite deformation radius, the dispersion relation for the Rossby wave can be expressed as

$$\omega = \frac{k(A(k^2 + l^2)^2 - \beta)}{(k^2 + l^2)^2 + \frac{1}{L_d^2}} = Ak - k\frac{\beta + A\frac{1}{L_d^2}}{(k^2 + l^2)^2 + \frac{1}{L_d^2}} \tag{3.9}$$

and the phase speed and group velocity component in zonal direction can be expressed as

$$c_x = A - \frac{\beta + A\frac{1}{L_d^2}}{(k^2+l^2)^2 + \frac{1}{L_d^2}} = \frac{A(k^2+l^2)^2 - \beta}{(k^2+l^2)^2 + \frac{1}{L_d^2}} \tag{3.10}$$

$$c_g = A + \frac{(\beta + A\frac{1}{L_d^2})(k^2 - l^2 - \frac{1}{L_d^2})}{(k^2+l^2+\frac{1}{L_d^2})^2} \tag{3.11}$$

It is important to note that mean velocity field is no longer just a shift in group velocity and phase speed, as we observed for the case of infinite deformation radius. Both terms, expressed in the equations above, are dependent on the mean flow of the fluid. Similarly for both cases, when A = $\beta/(k^2+l^2)$, the Rossby waves are stationary. A noticeable difference between the cases is observed when background flow is zero, A = 0, as the background flow still gives rise to changes in potential vorticity, due to the presence of the $1/\mathrm{L}_d^2$ term corresponding to large changes in the stream function. Since the region is no longer infinite, the potential vorticity equation has to be taken into account. If the westward group velocity consists of a wavenumber k (x-direction), that is small relative to wavenumber l (y-direction), then the phase speed will always have a westward propagation.

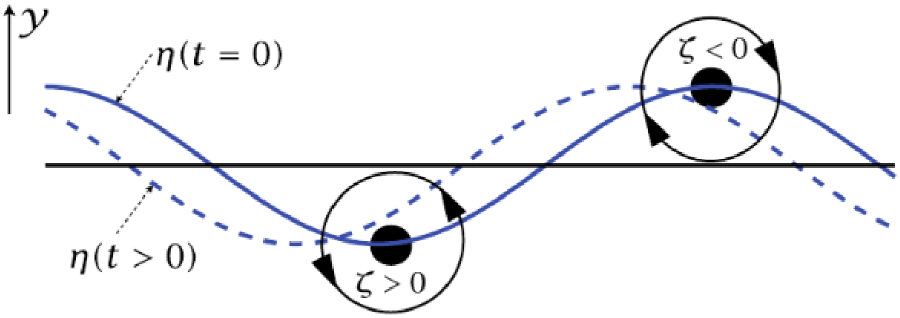

Figure 3.2: Westward propagation of Rossby waves, where solid black line represents the initial material line, solid blue line represents material line after a disturbance and blue dashed line represents evolution of the material line due to conservation of potential vorticity (18, p. 230).

A simple illustration considering Rossby wave propagation, that is induced by the conservation of potential vorticity, can be seen in Fig. 3.2. We consider some parcels, that are assumed to be at a constant arbitrary mid-latitude, and let them be affected by disturbance that induces changes in the Coriolis parameter. Changes in Coriolis parameter, as a response to the conservation of the potential vorticity, will result in a positive relative vorticity change, assuming that the disturbance was moving the parcels towards the south, or in negative relative vorticity change, assuming that the disturbance was moving the parcels towards the north. All of this combined lead to the westward Rossby wave propagation (18).

3.2.2 Mid-latitude cyclones

In addition to planetary scaled Rossby waves affecting mid-latitude atmospheric circulation, we also find cyclones, that are classified to be synoptic scaled weather systems. Even though cyclones can form both in the tropics and the mid-latitudes, for the purpose of this thesis we are interested in mid-latitude cyclones, specifically the development of cold core baroclinic cyclones.

Mid-latitudes are characterised by a baroclinic atmosphere and the strong temperature gradient between tropical and polar regions, giving a rise to the jet stream. Instabilities of the jet stream flow in the mid-latitudes (the consequence of baroclinic instability) cause extra-tropical cyclones or baroclinic eddies. The energy that drives the extra-tropical cyclone is derived from the temperature contrast across the front which caused when a very cold air mass meeting a very hot air mass. In the mid-latitudes atmosphere, they exist as a synoptic-scale baroclinic systems with a cold core.

4

Data and Methods

4.1 ERA5 database

During this project we will be using ERA5 global reanalysis dataset, provided by European Centre for Medium-Range Weather Forecast (ECMWF) (14). ERA5 is an improved reanalysis dataset, that replaces well known and previously used ERA-Interim reanalysis database (11). By increasing both spatial and temporal resolutions, decreasing latency time and including uncertainty estimates, ERA5 reanalysis dataset provides more detailed data compared to the commonly used ERA-Interim database.

For the purpose of this thesis, most of the upcoming analysis will be based on the decomposition of geopotential height field data. ERA5 database provides both daily and monthly sampled data, that can be accessed for multiple different geopotential height field levels, where the 500 hPa and the 850 hPa geopotential height fields are the most commonly considered alternatives when analysing the atmospheric circulation. Even though ERA5 dataset is updated regularly, and originally extends from 1979 and to the present time, for the purpose of this thesis we consider the database to provide geopotential height field data that extends from 1st January 1979 and until 31st December 2021. Since we will analyse amplitude changes throughout the recent decades, it is preferable to have a dataset where sample points are a part of a full-year cycle, and therefore no data that has been recorded after 31st December 2021 will be considered.

4.2 Fourier series

Fourier series is a method that can be applied to study properties of a arbitrary periodic function. For instance, we can use the Fourier series to decompose a periodic function, calculate the Fourier coefficients and then analyse the amplitude and phase shift of waves of interest. The essential mechanism behind a Fourier series is expressing any chosen periodic function as a sum of of multiple sine and cosine waves, that are also referred to as harmonics. By combining multiple harmonics provided by the Fourier series, we can reproduce the original function shape, further tested and discussed in section 5.1.

Since Fourier series are based on sine and cosine functions, we can use several different trigonometric identities to achieve several different forms of Fourier series. The most known forms of Fourier series are the sine-cosine Fourier series and the amplitude-phase Fourier series. Following the definition of Fourier series, we can express the sine-cosine form of Fourier series as

$$G(x) = \frac{a_0}{2} + \sum_{n=1}^{N} a_{\mathrm{n}} \cos\left(\frac{2\pi}{L} nx\right) + b_{\mathrm{n}} \sin\left(\frac{2\pi}{L} nx\right) \tag{4.1}$$

where $G(x)$ is a real-valued periodic function, L is the period of the function, n is the integer index representing the frequency of each harmonic, and a_0, a_n and b_n are Fourier coefficients, here expressed using Cartesian coordinates. By performing further harmonic analysis, we find that these Fourier coefficients can be expressed as

$$a_0 = \frac{2}{L} \int_L G(x)\, dx \tag{4.2}$$

$$a_n = \frac{2}{L} \int_L G(x) \cos\left(\frac{2\pi}{L} nx\right) dx \tag{4.3}$$

$$b_n = \frac{2}{L} \int_L G(x) \sin\left(\frac{2\pi}{L} nx\right) dx \tag{4.4}$$

To transform the sine-cosine form of Fourier series into the form of amplitude-phase Fourier series, we use trigonometric identities. By considering Ptolemy's theorem and the following cosine addition trigonometric identity, we can combine the sine and cosine terms provided in eq. 4.1 into a single cosine term. The general cosine addition trigonometric identity, regarding two arbitrary coefficients C and D, can be expressed as

$$\cos(C - D) = \cos(C)\cos(D) \; + \; \sin(C)\sin(D) \tag{4.5}$$

By assuming a right triangle, where the sides can be expressed as a_n, b_n and $\sqrt{a_n^2 + b_n^2}$, and defining a new coefficient $\phi_n = \tan^{-1}(b_n/a_n)$, we express the trigonometric identity provided in eq. 4.5 as

$$\cos\left(\frac{2\pi}{L}nx - \phi_n\right) = \cos\left(\frac{2\pi}{L}nx\right)\cos(\phi_n) \; + \; \sin\left(\frac{2\pi}{L}nx\right)\sin(\phi_n) \tag{4.6}$$

By inserting for ϕ_n into sine and cosine terms in the equation above, and defining a new constant $A_n = \sqrt{a_n^2 + b_n^2}$, we rewrite eq. 4.1 as the amplitude-phase Fourier series equation:

$$G(x) = \frac{A_0}{2} + \sum_{n=1}^{N} A_{\mathrm{n}} \cos\left(\frac{2\pi}{L}nx \; - \; \phi_n\right) \tag{4.7}$$

Due to properties of a harmonic, the earlier defined A_n and ϕ_n coefficients respectively represent the amplitude and the phase shift of the corresponding harmonic.

4.2.1 Fourier decomposition of a geopotential height field

The general principles of Fourier series can be applied to any periodic function, including the geopotential height field, that can be decomposed as a sum of multiple atmospheric waves.

We define a geopotential height field, $\Phi(t, \phi, \theta)$, where t is time, ϕ is latitude and θ is longitude. By integrating over all longitudes, we define the geopotential height field data to be periodic and dependent on latitude and time. Since our periodic function is latitude depending, we know that the period of our function is $L = 360$, and we can therefore rewrite the general sine-cosine series, eq. 4.1, and general Fourier coefficients, eqs.: 4.2, 4.3 and 4.4, as

$$\Phi(t,\phi) = \frac{a_0}{2} + \sum_{n=1}^{N} a_{\mathrm{n}} \cos\left(\frac{2\pi n}{360}\,\phi\right) + b_{\mathrm{n}} \sin\left(\frac{2\pi n}{360}\,\phi\right) \tag{4.8}$$

By using harmonic analysis, and following the same procedure as in the general case described earlier, we can calculate the Fourier coefficients and the atmospheric wave amplitude and phase shift.

5

Fourier Series implementation

5.1 Fourier Decomposition of 500 hPa geopotential height field

As previously discussed in section 3.2.1, Rossby waves are an essential part of mid-latitude climate. Distribution of cold polar and warm tropical air are the basis of atmospheric Rossby wave meandering, and are one of the main reasons defining mid-latitude climate. Therefore, analysing atmospheric Rossby waves in more detail will provide us with higher understanding of mid-latitude climate and its changes. To analyse the properties of atmospheric Rossby waves, we will use Fourier decomposition on geopotential height field data provided by the ERA5 database. Since the ERA5 database has many different geopotential height field levels included, we have to decide which of the geopotential height fields we want to decompose and analyse, with 500 hPa and 850 hPa geopotential height falling as natural choices when working with waves in the atmospheric circulation. An important factor to consider when making the decision is the disturbances in the atmospheric circulation. Since topography is one of the main Rossby wave sources, we know that topography is going to be affecting both geopotential height fields. However, since the 500 hPa geopotential height field is located at a higher altitude, $\sim 5\,500$ m above the surface, while the 850 hPa geopotential height field is located a lower altitude,

$\sim$ 1 500 m above the surface, we know that 850 hPa geopotential height field experiences larger influence caused by higher local features. Thus, the 500 hPa geopotential height field is more representative of the large-scale atmospheric circulation.

Fourier decomposition of the geopotential height field will provide information regarding amplitude, wave number and phase of Rossby waves, as described in section 4.2. However, before further analysis, it is important to confirm that the Fourier decomposition of the geopotential height field is implemented correctly and provide valid results. A possible method for result confirmation is to take the Fourier decomposition of a signal of choice and examine if we are able to recreate the original signal shape by summing up multiple harmonics provided by Fourier series. In our case, we plot the geopotential height field as a function of latitude, and try to recreate the original function shape by implementing the sine-cosine Fourier series discussed in section 4.2:

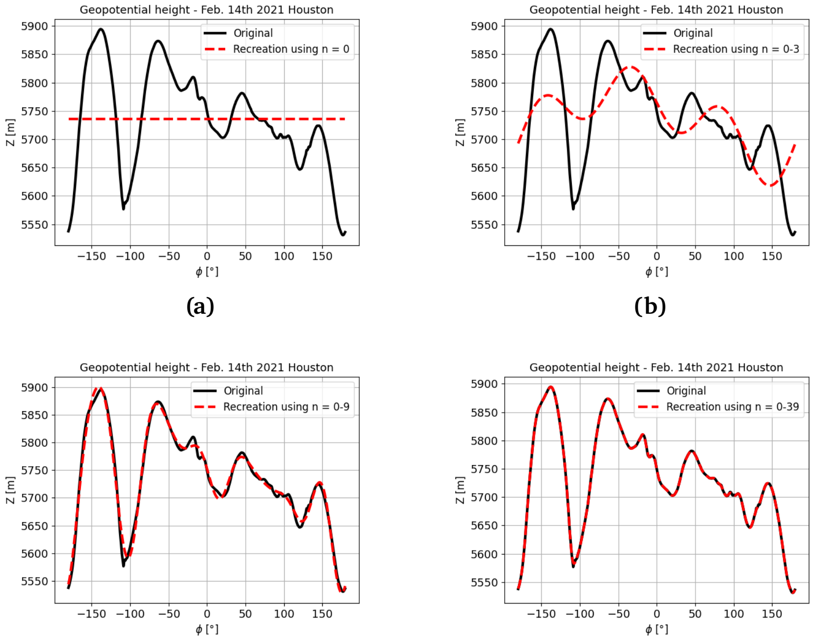

(a) (b)

(c) (d)

Figure 5.1: Reconstruction of geopotential height field function. Black solid line indicates the original geopotential height as a function of latitude, while the red dashed line indicates the reconstructed signal. Signal reconstruction is calculated by summing up first n scaled sine and cosine harmonics, where higher choice of n provides more accurate signal reconstruction. This is illustrated by reconstructing the signal where in (a) use only the mean value of the zonal flow provided by n = 0, (b) take the sum of functions provided by n = 0-3, (c) take the sum of functions provided by n = 0-9, and (d) take the sum of functions provided by n = 0-39.

From the figure above, it is clear that the recreation of the original function, where we sum the sine and cosine harmonics provided by the implemented Fourier series, was successful. Thus, we will from here on now use the corresponding Fourier series implementation when decomposing atmospheric Rossby waves.

5.2 Time Series Analysis

Before going into further amplitude analysis, we have to analyse the properties of the time series of interest. Throughout this thesis we will mainly consider waves with wavenumber 1-3, with detailed reasoning provided in section 6.1, and for the simplicity we will refer to wave corresponding to wavenumber 1 as case 1, wave corresponding to wavenumber 2 as case 2, and wave corresponding to wave number 3 as case 3.

We will now take a closer look at daily geopotential height field data provided by ERA5, and calculate daily wave amplitudes for entire time series data. The ERA5 database provides us with daily geopotential height field data between the 1st of January 1979 and the 31st of December 2021, yielding a total of 15 706 individual sample points for our analysis. Figure 5.2 illustrates the time series for case 1, where daily wave amplitudes are expressed as a function of time.

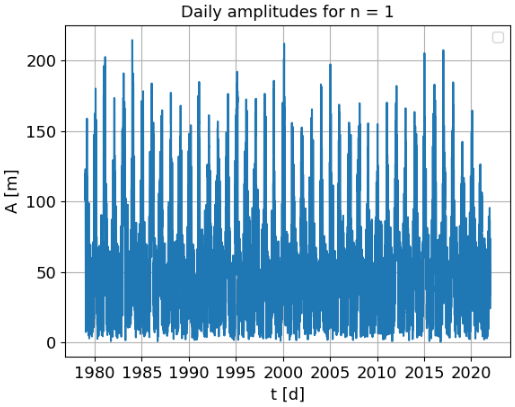

Figure 5.2: Case 1: daily Rossby wave amplitudes as a function of time. Planetary wave amplitudes vary in magnitude throughout the year, with highest amplitudes during the winter months, and lowest amplitudes during the summer months.

Working with time series data can be complicated, specially considering analysis of a non-stationary time series. Figure 5.2 confirms that the wave amplitude time series, analysed throughout this theses, is non-stationary, as we can observe a significant seasonal amplitude variations. Removing seasonal amplitude variations would be beneficial, as the resulting time series could potentially be approximated to be stationary, leading to simplified mean and standard deviation value calculations.

When calculating the seasonal cycle, we can either use the monthly sampled geopotential height field data or the daily sampled geopotential height field data provided by ERA5. Using the monthly sampled geopotential height field data would be most efficient, as the total number of sample points is much smaller compared to the daily sampled geopotential height field data. Optimally, we would hope that both of the daily and monthly sampled geopotential height field data would provide approximately same seasonal cycle, such that the most efficient dataset could be chosen for future analysis. To test if using daily and monthly sampled data has any affect on the total seasonal cycle, we calculate a seasonal cycle using each of the datasets for all three cases, and compare the differences, see fig. 5.3. The results for all three cases have the same tendency: seasonal cycle based on daily geopotential height field data indicates that seasonal amplitude variation is of higher magnitude compared to the seasonal cycle based on monthly geopotential height field data. While the amplitude difference between seasonal cycles during the winter days can be as low as $\approx$ 3 m, summer days indicate a larger difference, where the amplitude can differ by more than 10 m. Since the amplitude variation tendency while comparing the seasonal variation cycles between the datasets stays the same for all three cases, it implies that the datasets do not produce approximately same seasonal cycle, and requires further analysis.

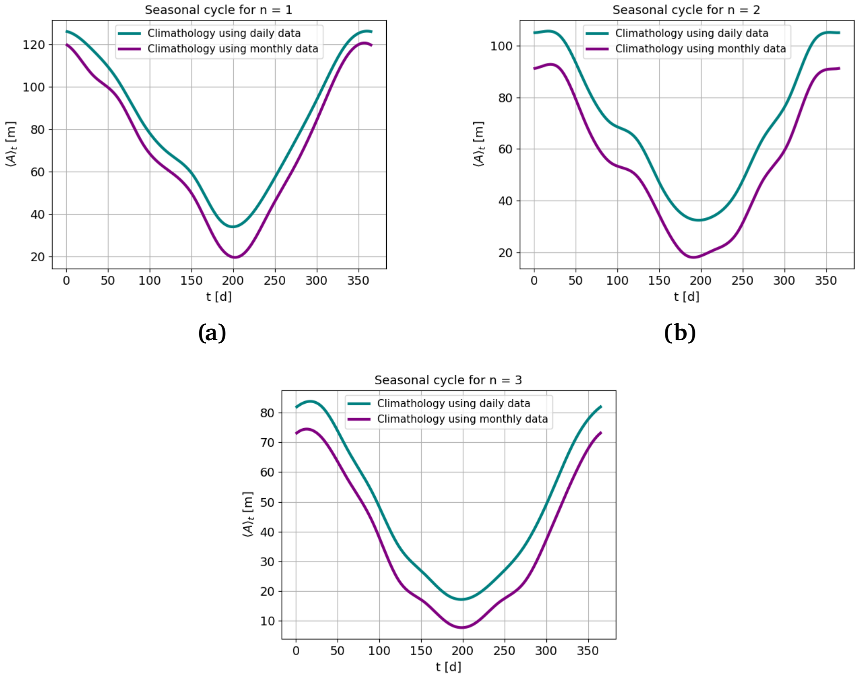

(a) (b) (c)

Figure 5.3: Mean seasonal amplitude variation cycle throughout one year, where day 0 represents 1st of January and day 356 represents 31st of December. Blue solid line represents seasonal cycle calculated using daily geopotential height field data, while purple solid line represents seasonal cycle calculated using monthly geopotential height field data. Seasonal amplitude variation cycles are calculated for (a) case 1, (b) case 2 and (c) case 3. Seasonal cycles calculated with daily data indicate higher seasonal amplitude variation for all three cases.

Even though seasonality calculated with daily geopotential height field data indicates that seasonal amplitude variations are higher than variations indicated by the seasonality calculated with monthly geopotential height field data, it does not necessarily indicate that it has a more accurate representation. To decide which of the seasonal cycles is a more accurate representation, further analysis is required. For each case, we subtract the seasonality from the original daily amplitude time series, such that in theory we should be left with a time series where the data mean is normalized around 0. Since we are working with a daily time series that extend over 42 years, we have to consider leap years. Our seasonal cycle is calculated as a function of 366 time steps, that represent the 366 days in a leap year. Therefore, no further corrections has to be made when we subtract the seasonal cycle from the the years containing 366 days. When subtracting the seasonal cycle from years containing 365 days, we skip the amplitude value representing the 29th of February. If we then assume that our time series data is stationary and follow normal distribution, we can calculate the values for the mean, one standard deviation (1xSTD), two standard deviations (2xSTD) and three standard deviations (3xSTD) of our time series, considering each of the seasonal cycles presented in fig. 5.3, see figs. 5.4, 5.5 and 5.6.

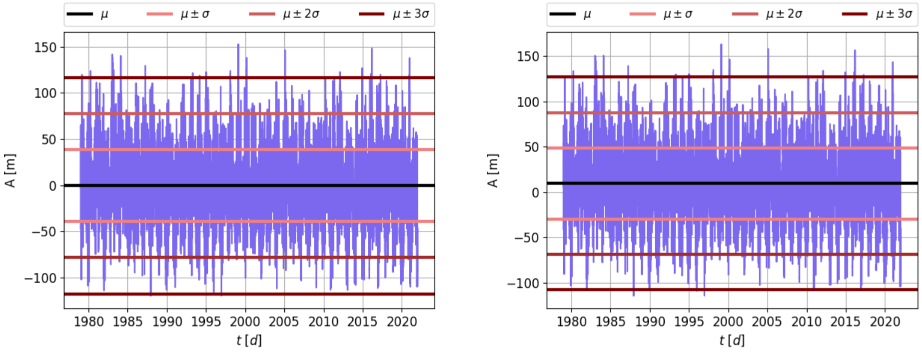

(a) **(b)**

Figure 5.4: Case 1: Daily amplitude time series after removal of seasonal amplitude variations. (a) Time series after removal of seasonal cycle calculated using daily geopotential height field data, and (b) time series after removal of seasonal cycle calculated using monthly geopotential height field data. Black solid line indicates the mean of the data, while coral, pink and dark red solid lines represent 1xSTD, 2xSTD and 3xSTD values from the mean respectively, see table 5.1.

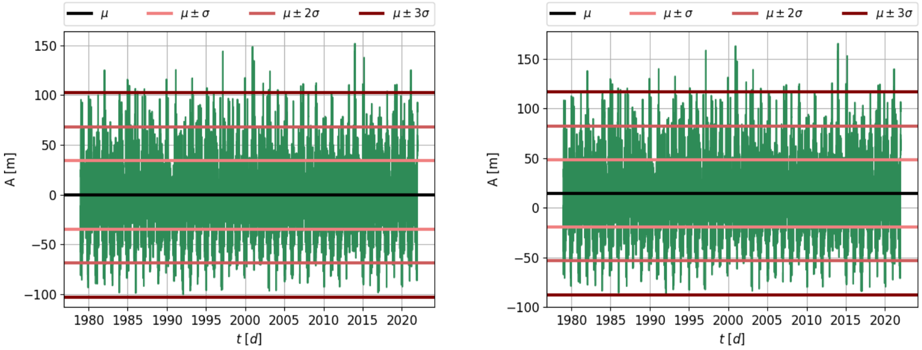

(a) **(b)**

Figure 5.5: As fig. 5.4, but for case 2 wave.

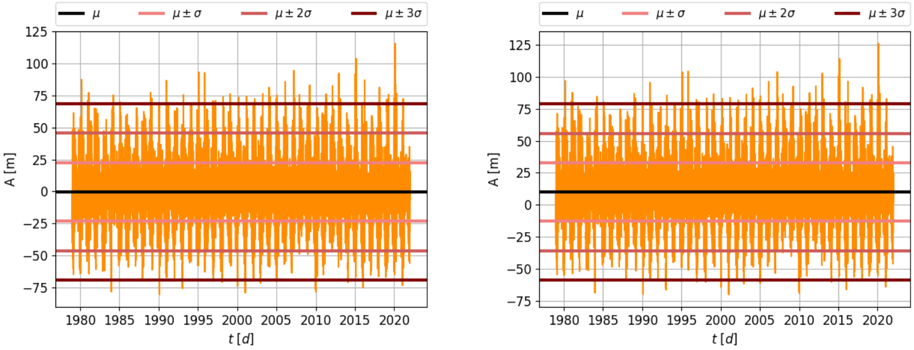

(a) **(b)**

Figure 5.6: As fig. 5.4, but for case 3 wave.

Since the mean of our time series data, after the seasonality removal, should theoretically lay at ≈ 0, we can compare the different mean values from figs. 5.4, 5.5 and 5.6, examine which of them are closest to our expectation and decide which seasonal cycle representation should be used for future analysis. Table 5.1 represents the mean, 1xSTD, 2xSTD and 3xSTD values for all three cases.

Table 5.1: Mean and 1xSTD, 2xSTD and 3xSTD values from figures 5.4, 5.5 and 5.6 for all three cases. Mark that this table represents original standard deviation values, while figures represent standard deviation values from the mean amplitude value. A_m is the amplitude after monthly seasonal cycle removal, A_d is the amplitude after daily seasonal cycle removal and σ, 2σ and 3σ are the 1xSTD, 2xSTD and 3xSTD values respectively.

Case 1				
	μ	σ	2σ	3σ
A_m	9.7	39.1	78.3	117.4
A_d	- 0.3	39.0	78.1	117.1

Case 2				
	μ	σ	2σ	3σ
A_m	14.4	34.0	68.0	102.1
A_d	- 0.3	34.1	68.3	102.4

Case 3				
	μ	σ	2σ	3σ
A_m	10.0	22.9	45.8	68.7
A_d	- 0.3	22.9	45.9	68.8

Based on the mean and standard deviation values provided by table 5.1, we notice a clear tendency throughout all three cases. Both 1xSTD, 2xSTD and 3xSTD values are approximately equal for both time series, implying that amplitude variations in different seasonal cycles has little affect on calculation of standard deviation values. However, considering the mean of both time series, the choice of seasonal cycle highly affects the corresponding data mean value. Looking at the time series where we subtract the seasonal cycle calculated with daily geopotential height field data, the data mean falls right under 0, that again falls in the proximity of our expected data mean value. On the other hand, when we look at the time series where we subtract the seasonal cycle calculated by monthly geopotential height field data, the data mean ranges between $\approx$ 10-14 for the three different cases. As discussed previously, our expected data mean should be ≈ 0, implying that time series that is subtracted by the daily calculated seasonal cycle provides more accurate results for all three cases. Therefore, analysis in this thesis will be computed using daily amplitude time series, where seasonality removal is based on the seasonal cycle calculated using daily geopotential height field data, see fig. 5.3. Removal of a possible linear trend throughout the time series data was tested as well, yielding no changes in the results.

6

Rossby Wave Changes During Recent Decades

6.1 Rossby Wave Amplitude Analysis for February 2021 Cold Spell Event

In chapter 4, we looked into how Fourier decomposition provides Fourier coefficients, a_n and b_n, and how they can be used in amplitude and phase calculations. These coefficients depend on the choice of n, which is the zonal Rossby wavenumber, hereby allowing for amplitude and phase calculations of individual waves with different wavenumbers. Waves can be split into different categories, depending on their wavenumber: waves with wavenumbers 1-3 are most commonly regarded as the planetary Rossby waves, while waves with wavenumbers 4-10 are most commonly regarded as synoptic waves (18). In addition, even though wavenumber 0 is not a wave in itself, it provides the mean of the zonal flow, as previously illustrated in Fig. 5.1. While separating between waves of different wavenumbers mathematically seems simple, as it depends on the choice of n in the Fourier analysis, it is also possible to separate between waves of different wavenumbers by studying the isolines of a geopotential height field. Studying the shape of geopotential height field isolines around a latitude circle, and considering the number of crests and troughs, tell us the wavenumber of the corresponding wave; in other words, the number of total crests and troughs of the isoline correspond to the wavenumber. For example, a wave consisting of one crest and one trough will have wavenumber 1, while a wave consisting of three crests and three troughs will gave wavenumber 3 and so on.

Previously, we considered a cold spell event taking place between 13th-17th of February 2021, and calculated surface air temperature anomalies that suggested the existence of a cold spell event. Now, we will take a further look at Rossby wave amplitude during the cold spell event, and examine if there are noticeable amplitude changes when comparing averaged cold spell event amplitude to the amplitude climatology. Figure 6.1 shows the average wave amplitude for waves of wavenumber 1-4 during the cold spell event, together with the corresponding amplitude climatology calculated using 1979-2020 February geopotential height field data. For the purpose of this thesis, we are only interested in the amplitude of waves with low wavenumber, since these are the planetary waves that could be responsible for cold polar air propagation towards the lower latitudes, even though waves of higher wavenumbers could be playing a role as well. If wave amplitude at a arbitrary time period is higher compared to the climatology of the same area, it indicates that the wave crests are reaching higher latitudes and wave troughs are reaching lower latitudes than usual for the same area. Since planetary waves are transporting cold polar air towards latitudes indicated by the wave troughs, and warm tropic air towards latitudes indicated by the wave crests, a change in wave amplitude affects the location of cold/warm air transportation. In other words, the mid-latitude climate can be highly affected by changes in planetary wave amplitude, specially considering latitudes that e.g. suddenly experience cold polar air transportation as a consequence of the wave through reaching lower latitudes than usual.

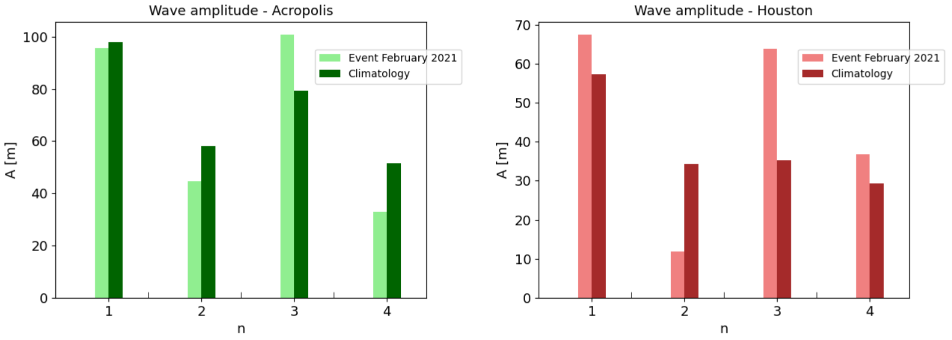

(a) **(b)**

Figure 6.1: Comparison between averaged wave amplitude for February 2021 cold spell event and amplitude climatology, illustrated for the first four wavenumbers. The bar with lighter color shading indicates the average cold spell amplitude, while the bar with darker color shading indicates the February amplitude climatology. The wave amplitude comparison is illustrated for latitudes corresponding to (a) Acropolis (38.0°latitude), and (b) Houston (30.0°latitude), where x-axis indicates the wavenumber and y-axis indicates amplitude in meters.

By looking at the figure above, we do not notice a clear trend in the amplitude anomalies when considering all of the wavenumbers together, but some of the individual wave numbers, specifically waves with wavenumbers 2 and 3, seem to have similar amplitude anomaly changes both in Acropolis and Houston. Wave amplitude throughout cold spell event is considerably lower for wavenumber 2, and remarkably higher for wavenumber 3, when comparing it to the amplitude of climatology for both Acropolis and Houston. This could indicate a possible significant increase in wave amplitude for wavenumber 3 could be the explanation for cold polar air supply at the latitudes of Acropolis and Houston, leading to unusually low temperatures and precipitation in the form of snow.

When considering wave amplitudes of wavenumbers 1 and 4, the cold spell event amplitudes appear to be lower in Acropolis, and higher in Houston, when compared to the corresponding climatology, however the significance in the amplitude difference cannot be concluded without further testing.

Considering that our main objective throughout this thesis is planetary wave amplitude analysis, we now concentrate on waves with wavenumber 1-3, defined as case 1, 2 and 3 respectively, as per definition these are the wavenumbers representing atmospheric Rossby waves. Until now, our calculations have been based on the latitudes of Acropolis (38.0° latitude) and Houston (30.0° latitude). Since the remarkable amplitude anomaly tendencies from the February

2021 cold spell event could be observed at both latitudes (Fig. 6.1), and the latitude difference between Acropolis and Houston is relatively small, we decide on a common latitude for each wavenumber by plotting the mean cold spell event amplitude as a function of latitude for each wavenumber, and choose the latitude that corresponds to the highest amplitude (Fig. 6.2). Some interesting additions, that due to lack of time could not be considered, would be to plot the climatology together with the plots in Fig. 5.3, as well as produce similar plots for a specific chosen latitude, where the x-axis could be replaced with time, and show the amplitude developments for a specific time frame.

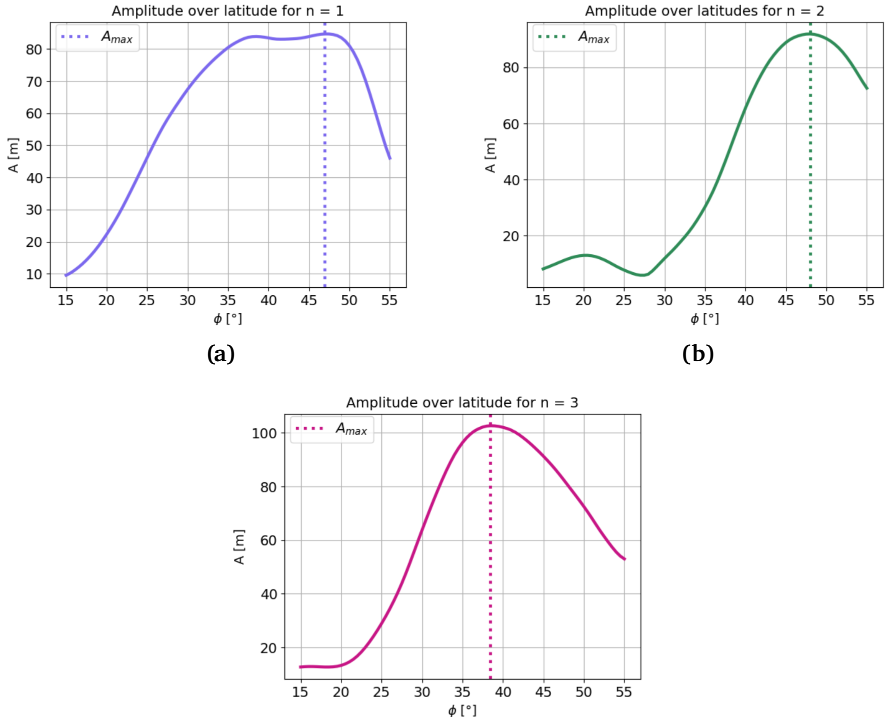

(a)

(b)

(c)

Figure 6.2: Averaged wave amplitude during February 2021 cold spell event as a function of latitude. The solid line represents wave amplitude as a function of latitude, and the dashed line represents the latitude corresponding to the highest amplitude, A_{max}. (a) Case 1: $A_{\text{max}} = 47.0°$ latitude, (b) case 2: $A_{\text{max}} = 48.0°$ latitude, and (c) case 3: $A_{\text{max}} = 38.5°$ latitude.

Further calculations will be based on the latitudes presented in Fig. 6.2: for case 1: 47.0° latitude, for case 2: 48.0° latitude, and for case 3: 38.5° latitude. It is important to note that the choice of latitude is based on the mean wave amplitude from February 2021 cold spell event, and therefore has a high dependence on the atmospheric conditions present in the time period of 13th-17th of

February 2021. Optimally, a better latitude selection method should have been considered, making the choice less dependent on a specific cold spell event. For instance, a latitude choice should rather have been based on the climatology data, and not a specific cold spell event data.

6.2 Analysis of Amplitude Anomalies in Mid-Latitude Regions

In this section we will examine Rossby wave amplitude tendencies throughout multiple predefined events and investigate potential event frequency and duration changes, based on daily wave amplitude time series provided in figs. 5.4(a), 5.5(a) and 5.6(a). We will perform trend analysis on all three cases, where subsection 6.2.1 will focus on trend analysis for case 1, subsection 6.2.2 will focus on trend analysis for case 2 and subsection 6.2.3 will focus on trend analysis for case 3. Since the analysis, calculations and the set up of results will stay the same for all three cases, subsection 6.2.1 will provide detailed method and calculation descriptions, in addition to the result analysis for case 1, while subsections 6.2.2 and 6.2.3 will only provide result analysis for case 2 and case 3. In the end, we will provide a short discussion regarding results for all three cases, and consider possible improvements.

Before further analysis, we have to define the events we would like to investigate further. We use the definition of standard deviation to define a event: considering daily amplitude time series, we know that $\approx 68.7\%$ of daily amplitudes has to fall within 1xSTD, $\approx 95.4\%$ of daily amplitudes has to fall within 2xSTD, and $\approx 99.7\%$ of daily amplitudes has to fall within 3xSTD (17). Table 6.1 shows how many days exceed the different standard deviation values, considering all three cases. The most interesting results are achieved by considering the most extreme cases, thus, we define that all anomalies exceeding 2xSTD value will be considered to be days representing an event, and all anomalies exceeding 3xSTD value will be considered to be days representing an extreme event. During this thesis, we will perform analysis regarding the amplitude anomalies on both event days exceeding the 2xSTD value, as well as extreme event days exceeding the 3xSTD value, considering all three cases.

Table 6.1: Number of days where daily wave amplitude is exceeding the 1xSTD, 2xSTD and 3xSTD values, presented in figs. 5.4(a), 5.5(a) and 5.6(a) for case 1, case 2 and case 3 respectively. Standard deviation values are provided by table 5.1 and 1σ, 2σ and 3σ are the 1xSTD, 2xSTD and 3xSTD values respectively. Time series data considered in the calculation extends over 15 706 days.

	Days over 1σ	Days over 2σ	Days over 3σ
Case 1	2 418	518	52
Case 2	2 345	556	69
Case 3	2 226	546	97

6.2.1 Case 1: Analysis of Waves with Wavenumber 1

Optimally, we would have considered the amplitude anomaly tendencies and linked them to cold spell events, but due to lack of time, no analysis regarding the temperatures could be performed, meaning to linkage to cold spells could be achieved. Thus, the events referred throughout this thesis should not be confused with cold spell events. However, since the original plan was to link amplitude anomaly tendencies to cold spell events, and to make possible linkage easier for further studies, we will consider events that use similar properties of the ones corresponding to cold spell events.

Even though we consider the total number of days where the wave amplitude exceeds the value of 2XSTD and 3xSTD as indicators of the days where an event could have taken place, the number of individual days do not represent the total number of events. First of all, number of days indicated in the table 6.1 are the total number of days exceeding the standard deviation values, where all of yearly seasons are considered. Since our goal is to investigate the frequency of events that could be directly compared to cold spells, we are not interested in the summer/spring days that fall between the months of May and September, but we rather want to consider only the fall/winter days that fall between the months of October and April. Therefore, of the total number of days that exceed the standard deviation value, see table 5.2, we discard all days between the months of May and September and keep only the days between the months of October and April.

Furthermore, an event can extend over multiple days, as it can take anywhere between 5-10 days before atmospheric circulation pattern changes. Thus there can be multiple days that exceed the standard deviation values that represent the same event. For an event to be considered as a new and separate event, we have to set a limit, and only if there has been more than a limited number of days since the standard deviation value has been exceeded last time, can the day belong to a new event. If there are less than predefined number of days since the standard deviation value has been exceeded last time, the day will be considered to belong to an already existing event.

To test for the best choice of day limit, we test it to be either 3, 5 or 7 days, and examine how number of events change together with the day limit. As one would expect, the number of events is highest when using 3 day limit for event classification, while the number of events is lowest when using 7 day limit for event classification. However, even though the total number of events varies, the magnitude of variations are low; e.g. considering 1980s, the total number of events throughout the decade is: 52 events when using 3 day limit, 44 events when using 5 day limit , 39 events when using 7 day limit. In addition, when calculating the average event amplitude for the 1980s, the difference in mean amplitude value is minimal. This implies that the choice between 3, 5 and 7 day limits will have minimal affect on mean amplitude calculations. A typical cold spell event can last between 2 and more than 6 days, where cold spell event that has a 2 day duration is considered to be a short cold spell event, and a cold spell event that has more than 6 day duration is considered to be a long cold spell event (19). Based on this information, and the fact that that we have already used 5 days as a duration of February 2021 cold spell event, see ch. 5.1, we will from now on base our total number of event calculations on a 5 day limit.

To analyse the frequency trend of the events, we split up our time series into decades, and use values provided by table 6.1 to calculate the number of events in each decade, see table 6.2. Since we do not have enough data to fully evaluate the frequency of events in the 1970s and 2020s, we mark these decades with a gray shading, as we have to be careful when comparing the number of the events in these two decades together with the number of the events in the 1980s-2010s.

Table 6.2: Case 1: number of events exceeding 2xSTD and 3xSTD values, building on results from table 6.1 and regarding the days in the time period of October-April. Given our definition of an event, multiple days exceeding 2xSTD and 3xSTD values can fall under the same event; in this case, multiple days that exceed standard deviation value in a time frame of 5 days are considered to belong to the same event. To qualify as an new event, there has to be more than 5 days since standard deviation value was exceeded last time. The gray shaded decades, 1970s and 2020s, are not representative regarding number of events in those decades, as there is not enough data measurements to evaluate these decades.

Decade	Events over 2σ	Events over 3σ
70s	2	1
80s	44	7
90s	39	5
00s	29	3
10s	33	6
20s	6	2
Total	153	24

Considering the frequency of events that exceed both the 2xSTD and the 3xSTD values provided in table 6.2, we do not observe any clear trend throughout the 1980s-2010s. The event frequency can not be considered as increasing, since the maximum of number of events was in 1980s and the number of events has decreased in both 1990s and 2000s. Event frequency can also not be considered to be stable, as the number of events vary significantly throughout the decades. And while the event frequency seem to be decreasing through 1980s-2010s, the sudden frequency increase in 2010s do not imply a stable decreasing trend. Therefore, we have to conclude that no specific event frequency trend can be concluded based on the data provided in table 6.2.

When considering the gray shaded decades in table 6.2, the number of events from these decades should not be directly compared to the remaining decades. Looking at the 1970s, calculations of event frequency are based on the data from one single year, 1979, and therefore generally does not provide any interesting information that could be used for decade comparison. For that reason, we will be neglecting the 1970s in our event amplitude analysis. Looking at the 2020s, calculations of event frequency are based on a two year dataset, 2020 and 2021. Even though the event frequency in 2020s does not provide any statistical value, the average event amplitude could provide interesting information, specially considering the magnitude of the average amplitude in 2020s compared to the earlier decades. For that reason we will use the data from 2020s in our mean event amplitude calculations, while keeping in mind that results will be based on a two year dataset.

Moving on, we calculate the average event amplitude in each decade, and analyse the amplitude trends throughout the decades. Due to our definition of an event, we know that each event can include a list of multiple days exceeding the standard deviation values. Before proceeding with our calculations, we want to find the amplitude of each event. There are two possible methods that can be used to decide the event amplitude; we can either choose the maximum daily amplitude from all the days included in the same event, and use that maximum amplitude as the event amplitude, or we can average over all daily amplitudes from all the days belonging to the same event, and use the average amplitude as our event amplitude. Both methods provide valid results, but for simplicity reasons we let the event amplitude be decided by the maximum daily amplitude in each event dataset.

By averaging over all amplitudes for each event for all of the decades, we calculate the total mean event amplitude for each decade, and define that the event day corresponding to maximum amplitude will be regarded as day 0. Since we are not only interested in the magnitude of the mean amplitude, but also the event duration, we average all daily amplitudes for the first 10 days that come before and after each event, where days leading up to an event are regarded as days -1 to -10, and the days after the event are regarded as days 1 to 10, see fig. 6.3.

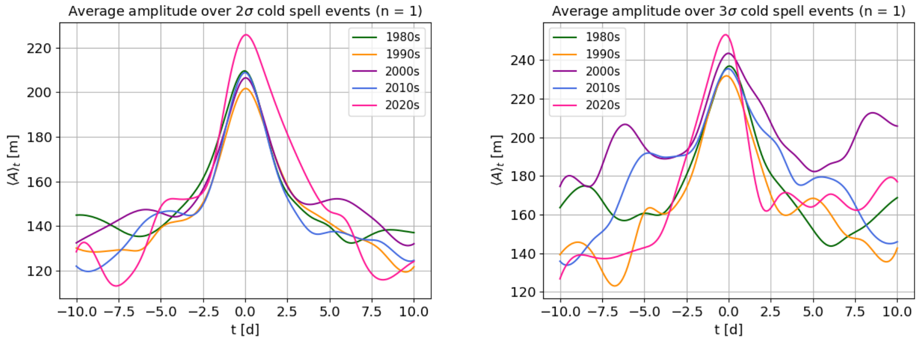

(a) **(b)**

Figure 6.3: Case 1: comparison of average event wave amplitudes throughout multiple decades (1990s - 2020s). Average wave amplitude is calculated separately for each decade, by averaging the amplitudes of all events that exceed the (a) 2xSTD value, and (b) 3xSTD value. Day 0 on the x-axis represents the day of the maximum wave amplitude in each event, and different colored solid lines represent different decades, as illustrated by the legend seen on the plots. The averaged wave amplitude values for each decade is presented in table 6.3.

When considering the average duration of events that exceed the 2xSTD value in each decade, we do not notice any specific trend between 1980s-2020s, see fig. 6.3(a). Considering the broadness of the amplitude functions representing the 1980s-2010s, we notice that the significant amplitude increase started ≈ 3 days before the event and that the corresponding amplitude decrease happened ≈ 3 days after the event, indicating that the duration of these events has stayed approximately constant throughout these decades. Considering the duration of events in the 2020s, it seems that the significant amplitude increase started ≈ 3 days before the events as well, and lasted until ≈ 5 days after the events. Even though the event duration has seemingly increased in 2020s compared to the remaining decades, these results are based on a incomplete dataset and therefore do not provide any certain conclusions, but rather some interesting observation.

When considering the duration of events that exceed the 3xSTD value, we notice clear variations throughout the decades, see fig. 6.3(b). Considering the broadness of amplitude functions throughout 1980s-2010s, we notice that the significant amplitude increase started ≈ 2.5-3 days before the event for all decades, while the timing of significant amplitude decrease varies with each decade. When considering the early decades, 1980s-1990s, the significant amplitude decrease took place ≈ 2.5-3.5 days after the event, while in the latter decades, 2000s-2010s, the significant amplitude decrease took place ≈ 4-5 days after the event. When considering the duration of the most extreme events, specifically the significant increase and decrease in wave amplitude, the results indicate that the average duration of events has increased throughout the decades.

We take a closer look at the magnitude of averaged event amplitudes for each decade, see table table 6.3. Just as in table table 6.2, we use gray shading for the 2020s, as these amplitude calculations depend on a dataset containing only 2 years of data.

Table 6.3: Case 1: averaged event wave amplitude values for each decade, as seen in fig. 6.3. The grayed out decade, 2020s, should not be directly compared to remaining decades, due to lack of data measurements. $\langle A \rangle_t$ is the averaged event wave amplitude, averaged over each decade, and 2σ and 3σ are the 2xSTD and 3xSTD values respectively.

Decade	$\langle A \rangle_t$ for events over 2σ [m]	$\langle A \rangle_t$ for events over 3σ [m]
1980s	209.6	236.9
1990s	201.7	231.8
2000s	206.5	243.5
2010s	208.8	235.5
2020s	225.8	253.1

From the values provided by table 6.3, we notice that the magnitude of the averaged amplitude in each decade is higher for events exceeding the 3xSTD value compared to the averaged amplitude for events that exceed 2xSTD. This is a nice way to check that our calculations correspond to our expectations, since by the definition of 3xSTD only the most extreme events should be considered, providing a higher mean wave amplitude value. We also notice that the amplitude values for the 2020s are significantly higher compared to the amplitude values for 1980s-2010s, indicating that the events in 2020s could be significantly more extreme than the average events is the decades before. However, we can not conclude that these high averaged amplitude values indicate an increasing amplitude trend for 2020s or have any significant statistical meaning, before more data is collected and evaluated, but it might be a basis for some interesting hypothesis regarding the amplitude magnitude of events in 2020s.

To study the event amplitude trend further, we perform a simple linear regression on the data provided by table 6.3, visualizing a potential underlying trend in the wave amplitude. We consider the trends based on two different datasets, where we either include or exclude the 2020s averaged amplitude data, see fig. 6.4. By excluding the 2020s in the linear regression, we are less biased by the incomplete 2020s dataset, and therefore expect more reliable results. However, it is still interesting to examine how the potential linear trend is affected by the inconclusive 2020s amplitude data.

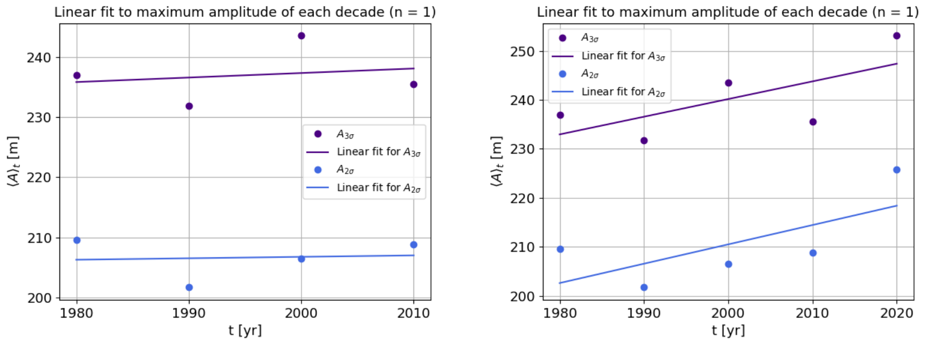

(a) **(b)**

Figure 6.4: Case 1: simple linear regression of the averaged wave amplitude values provided by table table 6.3. Linear regression is done considering: (a) averaged amplitude values, where the 2020s are excluded, and (b) averaged amplitude values, where 2020s are included. The dots are indicating wave amplitude values, while solid lines are indicating the corresponding linear fit calculated using linear regression. Blue color represents events that exceed the 2xSTD value and purple color represents events that exceed 3xSTD value.

For case 1, we observe a weak linearly increasing amplitude trend when excluding the data from 2020s, fig. 6.4(a), and a strong linearly increasing amplitude trend when including the data from the 2020s, fig. 6.4(b), both for events that exceed the 2xSTD and 3xSTD values. Considering the situation where 2020s data is included, we notice a significantly increasing linear trend, indicating that the average amplitude has increased by ≈ 20 m between 1980s-2020s. The rate and the magnitude of the linearly increasing amplitude seems to be unlikely high, and therefore might be an indicator to unreliable results when using the 2020s data.

For more conclusive results, we look at the situation where we exclude the 2020s data, fig. 6.4(a). Considering the events that exceed the 2xSTD value, we notice an approximately stationary linear trend, with a ≈ 1 m amplitude increase between 1980s-2010s. Considering the events that exceed the 3xSTD value, we observe a more noticeable linearly increasing trend, where the averaged wave amplitude has increased with ≈ 2-3 m between 1980s-2010s. This indicates that considering case 1, the most extreme events seem to have a weak linearly increasing amplitude trend, while no certain amplitude trend can be observed when considering all of the events together. Due to lack of time, no statistical significance analysis was performed on these discussed trends, and should be a priority when considering potential future work.

6.2.2 Case 2: Analysis of Waves with Wavenumber 2

Just as in previous subsection, we will analyse the event behavior, only for waves with wavenumber 2, also referred to as case 2. Table 6.4 represents the number of events that exceed the 2xSTD and 3xSTD values for each decade.

Table 6.4: As table 6.2, but for case 2 wave.

Decade	Events over 2σ	Events over 3σ
70s	2	0
80s	44	9
90s	32	5
00s	42	11
10s	40	9
20s	8	1
Total	168	35

Similar to case 1, we do not observe any specific frequency trends throughout the decades, as the number of events both increase and decrease with time without following any specific pattern. By averaging over amplitudes of events from table 6.4, we can illustrate the average amplitude magnitude and amplitude behavior for the days before and after each event, see fig. 6.5.

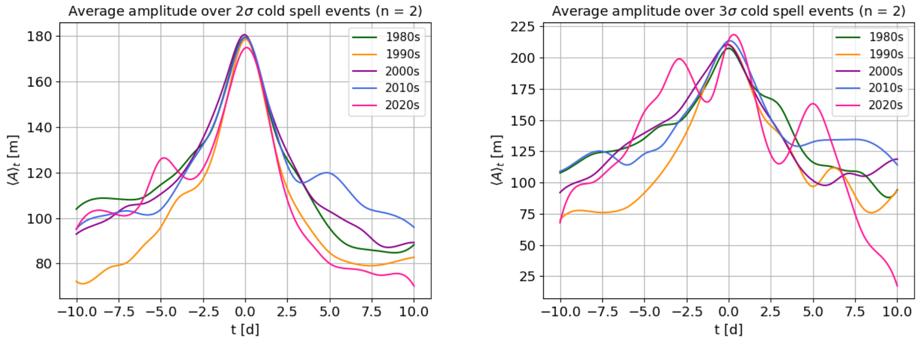

(a) **(b)**

Figure 6.5: As fig. 6.3, but for case 2 wave.

Considering events that exceed 2xSTD value, see fig. 6.5(a), the significant amplitude increase started ≈ 3-5 days before the event, and the significant amplitude decrease took place ≈ 3-5 days after the event. Even though the event duration seems to be shortest in 1990s and therefore might indicate that the duration of events has increased with time, the average event duration in 1980s being as long as the latter decades contradicts this hypothesis. Therefore just as in case 1, no significant trend can be concluded when considering the event duration.

On the other hand, considering events that exceed 3xSTD value while ignoring the 2020s, see fig. 6.5(b), significant amplitude increase and decrease took place at highly differing days throughout the decades, with 1990s seemingly having the longest event duration and the remaining decades having approximately similar event duration. Due to these results, and in contradiction to case 1, there seems to be no clear observable trend considering the duration of the most extreme events.

Table 6.5 highlights the averaged event amplitudes provided in fig. 6.5:

Table 6.5: As table 6.3, but for case 2 wave.

Decade	$\langle A \rangle_t$ for events over 2σ [m]	$\langle A \rangle_t$ for events over 3σ [m]
1980s	179.4	207.5
1990s	178.6	210.7
2000s	180.6	210.4
2010s	179.5	213.6
2020s	174.9	218.5

By performing simple linear regression on the values provided by table 6.5, we illustrate a possible underlying amplitude trend, see fig. 6.6:

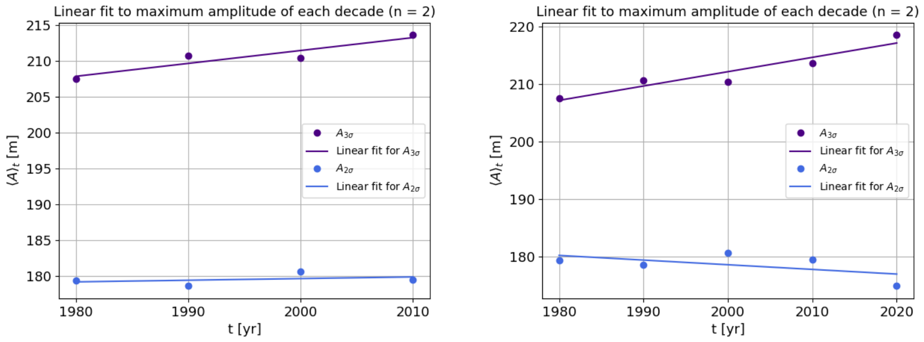

(a) **(b)**

Figure 6.6: As fig. 6.4, but for case 2 wave.

Considering the dataset that excludes the 2020s data, fig. 6.6(a), we notice a trend that corresponds to results from case 1. The amplitude of events that exceed the 2xSTD value increase with ≈ 1 m throughout the decades, indicating an extremely weak linearly increasing trend, that could be approximated as non-existent. The amplitude of events that exceed the 3xSTD values increase with ≈ 11 m throughout the decades, indicating a strong linearly increasing amplitude trend when regarding the most extreme events.

When considering the dataset that includes the 2020s data, fig. 6.6(b), the results are contradicting. We observe a linearly decreasing trend when considering all events together, and a strong linearly increasing trend when considering only the most extreme events. This tells us that the waves with wavenumber 2 were significantly weaker during events in 2020s in comparison to the waves with wavenumber 1, confirming the results previously provided in fig. 6.1. Just as with case 1, although the trends where 2020s data is included are interesting, they do not provide any significant conclusions and should not be considered statistically representative.

6.2.3 Case 3: Analysis of Waves with Wavenumber 3

At last, we analyse the events using waves with wavenumber 3, that we also refer to as case 3. The number of events in each decade are represented by table 6.6:

Table 6.6: As table 6.2, but for case 3 wave.

Decade	Events over 2σ	Events over 3σ
70s	5	0
80s	42	8
90s	45	12
00s	53	14
10s	46	14
20s	10	5
Total	201	53

The event frequency seems to contradict the results from case 1 and case 2, and seem to have a overall increasing frequency trend. While the frequency of events that exceed 3xSTD value have a clearly increasing trend, the trend is more arguable considering events that exceed 2xSTD value. Even though the event frequency seems to be consistently increasing throughout the 80s, 90s and 00s, the sudden frequency decrease in 10s contradicts the trend, and therefore does not allow us to make any accurate conclusions without further analysis.

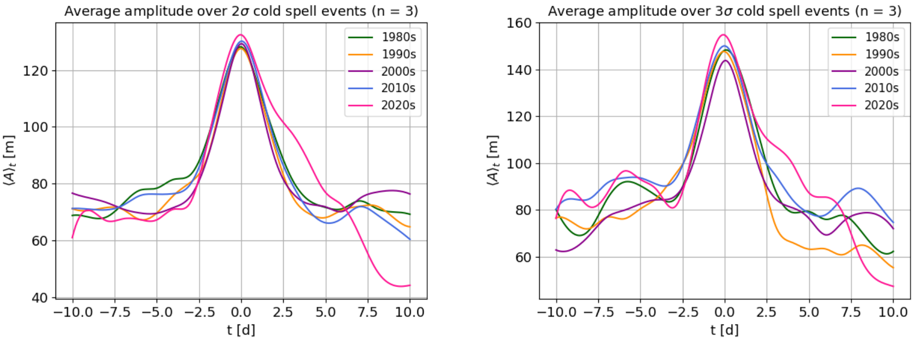

(a) **(b)**

Figure 6.7: As fig. 6.3, but for case 3 wave.

Figure 6.7 illustrates changes in averaged wave amplitude both before and after events for each separate decade. Considering both all events together (fig. 6.7b), and the most extreme events (fig. 6.7a), we see an indication that events seem to have a longer duration so far in 2020s compared to earlier decades. When comparing the 1990s-2010s, no clear event duration trends can be observed, as the events in all of these decades seem to have approximately equal duration.

Table 6.7 highlights the averaged event amplitudes provided in fig. 6.7:

Table 6.7: As table 6.3, but for case 3 wave.

Decade	$\langle A \rangle_t$ for events over 2σ [m]	$\langle A \rangle_t$ for events over 3σ [m]
1980s	128.2	148.3
1990s	127.6	147.7
2000s	129.3	143.8
2010s	130.2	150.1
2020s	132.4	154.8

To observe possible underlying wave amplitude trends, we perform linear regression on the values provided by table 6.7, see Fig. 6.8:

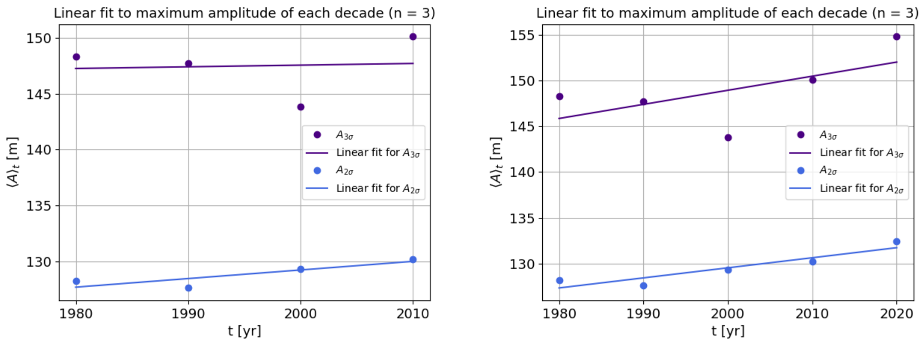

(a) **(b)**

Figure 6.8: As fig. 6.4, but for case 3 wave.

A clear linearly increasing trend can be observed for three of the situations presented in the figure above: considering the amplitudes during events that exceed 2xSTD value, where 2020s data is both included and excluded, and considering the amplitudes during events that exceed 3xSTD value where 2020s data is included. Just as in case 1, considering the dataset where 2020s are included, Fig. 6.8(b), we notice a strong linearly increasing amplitude trend, with an ≈ 5 m wave amplitude increase for events exceeding 2xSTD value and an ≈ 7 m wave amplitude increase for events exceeding 3xSTD value.

When considering dataset that excludes the 2020s data, fig. 6.8(a), we observe a linearly increasing amplitude trend, with an amplitude increase of ≈ 3-4 m, considering events that exceed 2xSTD value. On the other hand, when considering events that exceed 3xSTD value, we notice a extremely weak linearly increasing trend, with an amplitude increase of ≈ 0.5 m, where the amplitude tendencies could be approximated to be stationary throughout the decades. This contradicts to the results provided in case 1, fig. 6.4(a), and case 2, fig. 6.6(a), where amplitude changes considering the most extreme events indicated a clear linearly increasing trend. Considering case 3, we notice that linear regression provides a poor fit for the most extreme events, specially considering the low wave amplitudes in 2000s when compared to other decades, further discussed in section 6.2.4.

6.2.4 Possible Improvements of Case Analysis

Per our definition of an event, the event can take place between the months of October and April. This choice has a high effect on the averaged wave amplitude, since wave amplitude during summer months is much more lower compared to wave amplitude during winter months, see fig. 5.3. Therefore, including spring or fall months into our calculations can lead to a smaller averaged amplitude value, compared to the value that would be provided by averaging the amplitude provided by winter months alone. Including the months of April and October/November provides us with a larger and more diverse dataset to analyse, specially considering the recent cold temperatures that have been observed in Europe throughout April 2022 (10), however it could be argued that only the winter months should be considered.

In addition, analysis of amplitude changes and tendencies in this thesis are based on daily amplitude data that has been averaged over decades. This let us compare different decades to each other and provides with a simple and logical dataset split method. Also, when averaging over a longer period of time, in this case over 10 years, we make results less sensitive to possible short time disturbances. However, it could prove beneficial to split the data into a higher number of groups, for instance to split the data into sets of 3-5 years, and base our amplitude tendency analysis on that. When considering event duration, as in figs. 6.3, 6.5 and 6.7, we get a nice decade by decade comparison and more datasets are not necessary, while it would still provide with interesting information. However, when discussing event frequencies, as in tables 6.2, 6.4 and 6.6, as well as amplitude tendencies, as in figs. 6.4, 6.6 and 6.8, we are basing our analysis on a relatively small sample size, meaning our conclusions are not necessarily precise. For most accurate tendency representation, specially when considering methods as linear regression, a bigger data sample size could prove beneficial.

7

Summary & Future Work

7.1 Summary

In this thesis we studied the linkage between chosen events, that could potentially correspond to cold spells, and mid-latitude atmospheric circulation, specifically concentrating on atmospheric Rossby wave properties and their changes throughout the last four decades.

In chapter 3 we discussed the global atmospheric circulation, and the driving factors behind mid-latitude climate. By introducing large-scale planetary waves, their development and mechanics, we discussed how these atmospheric waves are an essential part of mid-latitude climate. In chapter 4 we discussed decomposition of atmospheric waves, and how it can provide important atmospheric wave properties, such as the wave amplitude, phase and wavenumber. In chapter 5, we analysed the 500 hPa geopotential height field using Fourier decomposition, and analysed the amplitude time series data. In chapter 6 we analyzed how Rossby waves have changed during the past decades, considering planetary waves of wavenumber 1-3.

By decomposing 500 hPa geopotential height field, we could analyse Rossby wave behaviour regarding three different cases, corresponding to waves of wavenumber 1, 2 and 3. Our goal was to analyze how frequency and duration of events, as well as wave amplitudes linked to these events, changed throughout multiple decades. Considering the analysis of 1980s-2010s data performed on these three case studies, overall results indicate that changes, and possible tendencies, between different decades are generally more noticeable when we studying events exceeding 3xSTD value compared to the events exceeding 2xSTD value. This indicates a possibility that there is a noticeable change in behavior of the most extreme events between separate decades, however more studies should be performed before drawing any certain conclusions.

When considering event frequency throughout the 1990s-2010s, as seen in tables 6.2, 6.4 and 6.6, no significant tendencies were observed regarding case 1 and case 2. Number of events changed from decade to decade, seemingly without any repeating patterns. Considering event frequency for case 3, there were indications that the number of events exceeding 3xSTD value increased with each decade, implying that the most extreme events could be becoming more common for this specific case.

Observing the event duration throughout 1980s-2010s, as seen in figs. 6.3, 6.5 and 6.7, we obtained differing results between the three cases. Considering events that exceed 2xSTD value, results from case 1 and case 3 indicate that the event duration have not had any significant changes throughout these decades, while results from case 2 indicate that the event duration differ throughout the decades, however without any clear pattern. When considering events that exceed 3xSTD value, results from case 1 indicate that the latter studied decades, 2000s and 2010s, indicate that events have an increased duration when compared to earlier decades, while results from case 2 and case 3 indicate no significant event duration changes or tendencies.

When studying changes in Rossby wave amplitudes associated with events throughout the 1990s-2010s, as seen in tables 6.3, 6.5, 6.7 and figs. 6.4, 6.6 and 6.8, and considering events exceeding 3xSTD value, we observed linearly increasing amplitude tendencies for case 1 and case 2, indicating that wave amplitudes linked with extreme events could be increasing in magnitude throughout decades. Results for case 3 did not share the same indications; even though a small amplitude increase throughout the decades was noted, it could not be concluded to have any significant statistical value. When considering events exceeding 2xSTD value, opposing tendencies were observed; results from case 1 and case 2 indicated no significant magnitude changes throughout the decades, while results from case 3 indicated a clear linearly increasing magnitude tendency.

In addition, we analyzed several situations where we included 2020s data into our calculations, such that possible indications of event behaviour throughout this decade could be observed. No certain conclusions can be drawn from these comparisons, as we compare events that happen in a time frame of 2 years with events that happened in a time frame of 10 years, however we did make some interesting observations. Results indicate that events so far in 2020s are linked to higher wave amplitude magnitude for all three cases, with the exception of events exceeding 2xSTD value in case 2. In addition, considering all three cases, results indicate that events so far in 2020s appear to have longer duration compared to the event duration in other decades. Furthermore, the number of events exceeding the 3xSTD value in case 1 and case 3 indicate a possibility for higher event frequency compared to other decades; for instance considering case 3, 5 extreme events have taken place in the first 2 years of 2020s, compared to the total of 8 events in 1980s and 14 events in 2010s, see table 6.6. By assuming that the rate of events in 2020s is going to be stable throughout the decade, the event frequency in 2020s could be expected to be higher compared to earlier decades.

7.2 Future Work

Based on results presented in this thesis, there are several natural ways to continue this research topic. First and furthermost, statistical significance of amplitude trends and tendencies presented during this should be examined. A common and well known approach would be to use the Monte Carlo approach, where statistical significance is calculated by comparing the time steps of interest with multiple randomly chosen time steps.

To confirm the suggested tendencies in our results, one could calculate and analyse the phase speed of Rossby waves that were analyzed throughout this thesis. As indicated by extreme event hypothesis, the increasing amplitude tendencies should result as a, among other things, response to slower wave phase velocities. By analyzing phase speed of waves of interest, one could compare if suggested increasing wave amplitude tendencies would correspond to decreasing phase speed tendencies of corresponding waves, providing a stronger confirmation to the extreme event hypothesis.

Another interesting topic for further research would be to investigate energy transport of the planetary waves analysed throughout this thesis. Based on the energy split method proposed by Graversen and Burtu (13), one could investigate how atmospheric energy transport is affected by planetary wave circulation changes and how it relates to the recent climate changes.

Bibliography

[1] Atmosphere and climate. `https://www.bbc.co.uk/bitesize/guides/zpykxsg/revision/1`. Accessed: 2021-12-09.

[2] Bangladesh faces 'worst flooding in 100 years' while climate talks in bonn falter. `https://www.independent.co.uk/climate-change/news/bangladesh-flood-climate-crisis-deaths-b2104922.html`. Accessed: 2022-06-21.

[3] Homeless people at risk of dying from extreme heat. `https://www.axios.com/2022/06/20/extreme-heat-homeless-people-deaths`. Accessed: 2022-06-21.

[4] In pictures: Greece's acropolis blanketed in snow. `https://www.bbc.com/news/world-europe-56089815`. Accessed: 2021-10-13.

[5] In pictures: Snow blankets greece and turkey after severe storm. `https://www.euronews.com/2022/01/25/in-pictures-snow-blankets-greece-and-turkey-after-severe-storm`. Accessed: 2022-06-21.

[6] In pictures: Snow blankets texas. `https://www.bbc.com/news/in-pictures-56083385`. Accessed: 2021-10-13.

[7] Layers of the atmosphere. `https://www.weather.gov/jetstream/layers`. Accessed: 2022-05-02.

[8] The link between biomes and climate. `https://www.thoughtco.com/what-are-biomes-1435312`. Accessed: 2022-04-11.

[9] New mexico wildfire leaves 2 dead and 200 structures damaged. `https://www.nytimes.com/2022/04/14/us/new-mexico-wildfire-deaths.html`.

Accessed: 2022-06-21.

[10] Record-setting cold snap hits europe, stunning spring crops. `https://www.washingtonpost.com/weather/2022/04/04/europe-record-cold-france-agriculture/`. Accessed: 2022-06-03.

[11] Dee, D. P., Uppala, S. M., Simmons, A. J., Berrisford, P., Poli, P., Kobayashi, S., Andrae, U., Balmaseda, M., Balsamo, G., et al. The era-interim reanalysis: configuration and performance of the data assimilation system. *Q. J. Royal Meteo. Soc.*, **137**:553–597, (2011). doi: 10.1002/qj.828.

[12] Francis, J. A. and Vavrus, S. J. Evidence linking arctic amplification to extreme weather in mid-latitudes. *Geophys. Res. Lett.*, **39(6)**, (2012). doi: 10.1029/2012GL051000.

[13] Graversen, R. G. and Burtu, M. Arctic amplification enhanced by latent energy transport of atmospheric planetary waves. *Q. J. Royal Meteo. Soc.*, **142(698)**:2046–2054, (2016). doi: 10.1002/qj.2802.

[14] Hersbach, H., Bell, B., Berrisford, P., Hirahara, S., Horányi, A., Muñoz-Sabater, J., Nicolas, J., Peubey, C., Radu, R., Schepers, D., et al. The era5 global reanalysis. *Q. J. Royal Meteo. Soc.*, **146(730)**:1999–2049, (2020). doi: 10.1002/qj.3803.

[15] IPCC. *Climate Change 2021: The Physical Science Basis. Contribution of Working Group I to the Sixth Assessment Report of the Intergovernmental Panel on Climate Change*. Cambridge University Press, (In Press).

[16] Kornhuber, K. and Tamarin-Brodsky, T. Future changes in northern hemisphere summer weather persistence linked to projected arctic warming. *Geophys. Res. Lett.*, **48(4)**:e2020GL091603, (2021). doi: 10.1029/2020GL091603.

[17] Lee, K., Dong, In, J., and Lee, S. Standard deviation and standard error of the mean. *Korean J Anesthesiol.*, **68(3)**:220–223, (2015). doi: 10.4097/kjae.2015.68.3.220.

[18] Vallis, G. K. *Atmospheric and Oceanic Fluid Dynamics: Fundamentals and Large-Scale Circulation, 2nd Edition*. Cambridge University Press, 2019.

[19] Wang, L., Liu, T., Hu, M., Zeng, W., Zhang, Y., Rutherford, S., Lin, H., Xiao, J., Yin, P., Liu, J., Chu, C., Tong, S., Ma, W., and Zhou, M. The impact of cold spells on mortality and effect modification by cold spell

characteristics. *Sci. Rep.*, **6**, (2016). doi: 10.1038/srep38380.